Article:
Zhang, B. orcid.org/0000-0002-0428-7745, Allegri, G. and Hallett, S.R. orcid.org/0000-0003-0751-8323 (2022) Embedding artificial neural networks into twin cohesive zone models for composites fatigue delamination prediction under various stress ratios and mode mixities. International Journal of Solids and Structures, 236-237. 111311. ISSN 0020-7683

https://doi.org/10.1016/j.ijsolstr.2021.111311

Accepted in the International Journal of Solids and Structures, 15 October 2021

Embedding artificial neural networks into twin cohesive zone models for composites fatigue delamination prediction under various stress ratios and mode mixities

Bing Zhang*, Giuliano Allegri, Stephen R. Hallett

Bristol Composites Institute, University of Bristol, Queen's Building, University Walk, Bristol BS8 1TR, UK

Abstract

This paper presents for the first time a novel numerical technique for modelling fatigue delamination growth in fibre reinforced composites, which is based on coupling two twin cohesive zone models with a single-hidden-layer artificial neural network. The simulation approach proposed here can describe composites fatigue delamination under negative & positive stress ratios and the full range of mode mixities. In the modelling strategy, each segment of a composites interface is described by two twin cohesive elements, which jointly provide local fracture mechanics parameters into a feedforward single-hidden-layer neural network, without the need to know the global load R ratio. In turn, the neural network algorithm feeds the fatigue crack propagation rate $\mathrm{d}a/\mathrm{d}N$ back into the twin cohesive elements, which follow a static and fatigue cohesive law in a synchronous fashion. The novel modelling methodology has been implemented in an explicit finite element scheme. The modelling strategy is first verified and validated by several benchmark cases, involving mode I Double Cantilever Beam tests, mode II End Loaded Split tests with and without reversal, as well as Mixed-Mode Bending tests. A relevant application of the modelling technique is demonstrated considering a tapered laminate, which experiences non-proportional loading due to the presence of combined static tension and cyclic bending.

Keywords: Cohesive zone model; Delamination; Fatigue; Finite element; Interface; Numerical methods

*Corresponding author: B.Zhang@bristol.ac.uk (Bing Zhang)

1. Introduction

Interlaminar debonding (delamination), usually initiating from free edges or manufacturing defects in a laminated composite, can significantly reduce the ultimate strength of fibre-reinforced plastic components. Mechanical fatigue may cause delamination to occur at a much lower strain level than under monotonic loading. Most composite structures are still designed based on a conservative 'no growth' philosophy, which means that the load level that a composite structure experiences throughout its service life is not allowed to exceed a critical maximum strain (e.g. ~4000 με), below which fatigue crack growth is unlikely to happen (Rouchon, 2009). The critical maximum strain is usually much lower than the ultimate load-bearing capability of the composite material. Consequently, in order to exploit the full potential of composites, crack-growth-based design approaches need to be adopted. This entails establishing accurate and robust numerical models for the prediction of fatigue delamination growth, especially because the experimental characterisation of fatigue damage is time-consuming and, hence, expensive.

The virtual crack closure technique (VCCT) (De Carvalho et al., 2019; Deobald et al., 2017; Krueger, 2004; Pirondi et al., 2014) and the level set method (Amiri-Rad et al., 2017; Latifi et al., 2015) have been widely employed for modelling fatigue delamination propagation in composite laminates. Since the pioneering work of Dugdale (Dugdale, 1960) and Barenblatt (Barenblatt, 1962), the concept of cohesive zone models (CZMs) has been extensively exploited within finite element (FE) analysis frameworks combined with damage mechanics. The past two decades have seen the extension of CZMs to fatigue delamination prediction (Bak et al., 2014; Pascoe et al., 2013). A relatively straightforward method of building fatigue CZMs entails globally loading a laminate model as in the actual tests and locally describing the full loading and unloading responses of cohesive interface elements. The loading-unloading hysteresis (LUH) approach requires describing the mechanical

response of a material throughout a whole cycle (Nojavan et al., 2016; Paepegem and Degrieck, 2001; Parrinello et al., 2021; Salih et al., 2018). A cycle jump strategy is usually needed in a LUH model to achieve a reasonable computational cost for the fatigue simulations (Nojavan et al., 2016; Paepegem and Degrieck, 2001). Large kinetic energies may be generated if the LUH method is implemented in an explicit FE scheme, thus the LUH method is more suitable for an implicit FE algorithm. The other approach of modelling fatigue via CZMs is globally loading the laminate in a static manner by following the maximum peak envelope of actual cycles (see Fig. 1a). The stiffness of cohesive elements is locally degraded according to combined static and fatigue cohesive laws, which are usually introduced as modifications of baseline static and bilinear CZMs (Bak et al., 2016; Carreras et al., 2019b; Dávila, 2020; de Moura and Gonçalves, 2014; Harper and Hallett, 2010; Iarve et al., 2017; Kawashita and Hallett, 2012; Pirondi and Moroni, 2019; Robinson et al., 2005; Tao et al., 2018; Turon et al., 2007), as illustrated in Fig. 1b. This approach, known as single load envelope (SLE), requires introducing an assumed number of fatigue cycles for a given time increment. This leads to the concept of 'numerical fatigue frequency', which is here defined as the number of cycles elapsed over one second in a fatigue model. The SLE approach has attracted considerable research interest, as it allows running simulations at a much higher numerical fatigue frequency than in actual tests, without triggering spurious kinetic effects, thus reducing the computational cost.

More recently, the load envelope approach has been extended to consider both the maximum and minimum load envelopes (Raimondo and Bisagni, 2020; Zhang et al., 2020a). The key advantage of a double load envelope (DLE) approach relative to a SLE approach is that the former allows evaluating the local strain energy release rate (SERR) or stress ratio via twin cohesive elements without the knowledge of global load R ratio, which is particularly useful when there is not direct correlation between the global R ratio and the

local fracture mechanics parameters. This is the typical case arising in non-proportional loading. However, it has not been demonstrated yet whether the DLE modelling approach works for a reversed fatigue case. Thus, one of the main objectives of this study is to extend the DLE modelling technique as developed in Ref. (Zhang et al., 2020a) to cover reversed, i.e. negative-stress-ratio, fatigue.

When both negative and positive stress ratios are considered in the twin CZMs modelling framework, it becomes more challenging to estimate the fatigue delamination growth rate ($\mathrm{d}a/\mathrm{d}N$) by using a the standard Paris law, as expressed in Eq. 1 (Bak et al., 2016; Carreras et al., 2019b; de Moura and Gonçalves, 2014; Harper and Hallett, 2010; Kawashita and Hallett, 2012; Raimondo and Bisagni, 2020; Tao et al., 2018; Turon et al., 2007; Zhang et al., 2020a):

$$\frac{da}{dN} = C[f(G_{\max}, \Delta G, G_C)]^m \tag{1}$$

where $G_{\max}$ is the maximum SERR, ΔG the SERR change and G_{C} the critical SERR for a given mode mixity; *C* and *m* are the Paris law pre-factor and exponent, which are in general functions of the stress-ratio and mode-mixity. In this respect, single-hidden-layer artificial neural networks (ANNs) offer a viable strategy for describing the dependency of the delamination growth rate on the ERR, as well as on the mode-mixity and stress-ratio (Allegri, 2018). This leads to the second novel contribution of the present paper, i.e. integration of a single hidden layer ANN into the twin CZMs framework.

In general, artificial neural networks, whose architectures mimic biological neural networks, have been employed to offer solutions to a wide range of engineering applications, in particular when it is difficult to derive analytical expressions describing the underlying material properties (Zhang and Friedrich, 2003). Once adequately trained, an ANN can simulate a complex non-linear information processing system via the weighted interconnections amongst neurons. Training of an ANN is achieved by adjusting the

interconnection weights until the prediction error is reduced to an acceptable level. ANNs have been successfully applied for evaluating the fatigue performance of composites, but mostly for stress-life curves (Diniz and Freire Júnior, 2020; El Kadi, 2006). Ref. (Allegri, 2018) presented the first study where ANNs were used to describe the fatigue delamination growth in composites. The ANN approach from Ref. (Allegri, 2018) is here embedded into the twin CZMs framework for fatigue delamination prediction.

A detailed description of the numerical framework that combines the double load envelope modelling approach and a feedforward neural network for fatigue delamination prediction will be given in Section 2. It is worth pointing out that the modelling technique introduced in this paper only considers constant amplitude fatigue, thus variable amplitude loading scenarios, e.g. (Erpolat et al., 2004; Jensen et al., 2021a, 2021b; Sarfaraz et al., 2013), are not covered in this study. The modelling strategy is then verified and validated in Section 3 through mode I Double Cantilever Beam (DCB), mode II End Loaded Split (ELS) with and without load reversal, and Mixed-Mode Bending (MMB) tests. Validation of a fatigue cohesive technique through these single-interface tests is essential before scaling it up towards multi-interface applications, as it was previously demonstrated for a SLE modelling approach (Tao et al., 2018). A typical application of the modelling methodology is demonstrated in Section 4, where we consider a tapered laminate under combined static tension and cyclic bending, i.e. a fatigue regime involving non-proportional loading.

2. Modelling technique

2.1 Overall framework

The fatigue delamination prediction strategy is illustrated in Fig. 2, considering a fully reversed mode II ELS fatigue case as an example. The composite laminate under analysis is virtually described by two twin FE models. During the load build-up stage, the twin models

are monotonically loaded to the trough and peak loads of the first cycle in a quasi-static manner, respectively. The twin models may need to be held for a period of time to reduce possible dynamic response before entering the fatigue stage (Harper and Hallett, 2010; Kawashita and Hallett, 2012). In the fatigue step, the twin models are respectively loaded following the trough and peak load envelopes of actual cycles (Fig. 2). The global loads on the models are kept synchronised throughout the whole numerical analysis, which can be easily achieved by defining the double load envelopes as functions of time in the FE package.

The twin FE models contain pairs of twin cohesive elements (e.g. element 1 and element 2 in Fig. 2) that are inserted between plies to predict delamination. Hence, each discretised segment of an interlaminar interface is jointly described by two twin cohesive elements; one represents the mechanical response of the interface segment at the peak load, whilst the other one describes the interface behaviour at the trough load. It is worth mentioning that cohesive elements could also be embedded along the fibre direction within plies to predict matrix failure if this is required (Mukhopadhyay et al., 2018; Tao et al., 2018). On top of the global load synchronisation between the twin models through the load envelopes, a local synchronisation is maintained between each pair of twin cohesive elements. The local synchronisation is enabled by a common static damage variable D_{s} and a common fatigue damage variable D_{f}, which are both jointly determined and shared by the twin elements. The twin cohesive elements communicate, to feed the local fracture mechanics variables (e.g. local SERR change between peak and trough loads) into a single-hidden-layer artificial neural network. The ANN in turn outputs estimated fatigue delamination growth rate into the twin cohesive elements (see Fig. 2), so that D_{f} can be calculated. Details of the cohesive formulation that integrates twin CZMs and the ANN are provided below.

2.2. Cohesive formulation

As previously mentioned, the cohesive formulation that was proposed in Ref. (Zhang et al., 2020a) for DLE-based modelling is here upgraded to cover the case of reversed fatigue via embedding an artificial neural network into the fatigue CZM.

2.2.1. Static formulation

The static bilinear cohesive law that provides the baseline for the fatigue formulation is firstly introduced by referring to Fig. 1b. The deformation of a cohesive element is described by three orthogonal displacement components (δ_{33}, δ_{13} and δ_{23}) in the element local coordinate system. The local axis 3 follows the element thickness direction, and the 1-2 plane is orthogonal to axis 3. The specific directions of axes 1 and 2 are not critical as the resultant in-plane shear displacement is used here for mode II displacement. The mode I opening displacement δ_{I}, mode II displacement δ_{II} and overall displacement δ_{m} are thus given by:

$$\delta_{\mathrm{I}} = \max(0, \delta_{33}); \qquad \delta_{\mathrm{II}} = \sqrt{{\delta_{13}}^2 + {\delta_{23}}^2}; \qquad \delta_{\mathrm{m}} = \sqrt{{\delta_{\mathrm{I}}}^2 + {\delta_{\mathrm{II}}}^2} \tag{2}$$

The ratios of mode I and II displacement components relative to the overall displacement are indicated by:

$$cosI = \frac{\delta_{\mathrm{I}}}{\delta_{\mathrm{m}}}; \qquad cosII = \frac{\delta_{\mathrm{II}}}{\delta_{\mathrm{m}}} \tag{3}$$

At the elastic stage, the twin cohesive elements are controlled by the mode I and II stiffness pair of the interface, K_{I} and K_{II}. This is mathematically expressed in Eq. 4, where σ_{I} and σ_{II} are mode I and mode II tractions.

$$\sigma_{\mathrm{I}} = K_{\mathrm{I}}\delta_{\mathrm{I}}; \qquad \sigma_{\mathrm{II}} = K_{\mathrm{II}}\delta_{\mathrm{II}} \tag{4}$$

When one of the twin cohesive elements is damaged according to the damage initiation criterion defined in Eq. 5, the other one will be forced to initiate damage (i.e. enter the softening region of the bilinear cohesive law in Fig. 1b). This guarantees the synchronisation of damage initiation between the twin cohesive elements. In Eq. 5, $\sigma_{\mathrm{I}}^{\max}$ is mode I strength; $\sigma_{\mathrm{II,E}}^{\max}$ is the enhanced mode II strength due to through-thickness compression (TTC), as

defined in Eq. 6. $\sigma_{\mathrm{II}}^{\max}$ is the mode II strength without TTC enhancement. η is the strength enhancement factor, which can be determined by experimental measurements (Gan et al., 2013):

$$\left(\frac{\max(0,\sigma_{\mathrm{I}})}{\sigma_{\mathrm{I}}^{\max}}\right)^2+\left(\frac{\sigma_{\mathrm{II}}}{\sigma_{\mathrm{II,E}}^{\max}}\right)^2=1 \tag{5}$$

$$\sigma_{\mathrm{II,E}}^{\max}=\sigma_{\mathrm{II}}^{\max}-\eta\cdot\min(0,\sigma_{\mathrm{I}}) \tag{6}$$

In the static stiffness degradation region of the bi-linear cohesive law, both elements are degraded using a common damage variable D_{s} (increasing from 0 at damage initiation to 1 at full failure), which ensures the local synchronisation in terms of interface static damage. The shared static damage variable is determined by the twin cohesive element that experiences the larger deformation. Mathematically, it can be expressed as the maximum of the transitional damage variables that are obtained by treating the twin elements separately:

$$D_{\mathrm{s}}=\max({}^{1}D_{\mathrm{s}},\ {}^{2}D_{\mathrm{s}}) \tag{7}$$

where ${}^{1}D_{\mathrm{s}}$ and ${}^{2}D_{\mathrm{s}}$ are two transitional damage variables. These two variables are separately calculated based on the deformation of the two twin elements by (Jiang et al., 2007):

$${}^{i}D_{\mathrm{s}}=\frac{\delta_{\mathrm{m}}-\delta_{\mathrm{m}}^{0}}{\delta_{\mathrm{m}}^{\mathrm{f}}-\delta_{\mathrm{m}}^{0}},\qquad i=1,2 \tag{8}$$

where δ_{m}^{0} and $\delta_{\mathrm{m}}^{\mathrm{f}}$ are the mixed-mode displacements at damage initiation and full failure, respectively. According to the initiation criterion in Eq. 5, δ_{m}^{0} can be derived in:

$$\left(\frac{K_{\mathrm{I}}\delta_{\mathrm{m}}^{0}cosI}{\sigma_{\mathrm{I}}^{\max}}\right)^2+\left(\frac{K_{\mathrm{II}}\delta_{\mathrm{m}}^{0}cosII}{\sigma_{\mathrm{II,E}}^{\max}}\right)^2=1 \tag{9}$$

The mode I and II yield strengths at failure initiation, i.e. (σ_{I}^{Y} and σ_{II}^{Y}) as indicated in Fig. 1b are thus achieved by:

$$\sigma_{\mathrm{I}}^{Y}=K_{\mathrm{I}}\delta_{\mathrm{m}}^{0}cosI;\qquad \sigma_{\mathrm{II}}^{Y}=K_{\mathrm{II}}\delta_{\mathrm{m}}^{0}cosII \tag{10}$$

A power law criterion is used for determining full failure, i.e.:

$$\left(\frac{G_{\mathrm{I}}}{G_{\mathrm{IC}}}\right)^{\alpha}+\left(\frac{G_{\mathrm{II}}}{G_{\mathrm{IIC,E}}}\right)^{\alpha}=1 \tag{11}$$

where G_{I} and G_{II} are mode I and mode II SERRs. Mode mixity $\emptyset$ is the ratio of mode II SERR (G_{II}) to the sum of mode I and II SERRs (G_{I} and G_{II}), $\emptyset = G_{\mathrm{II}}/(G_{\mathrm{I}} + G_{\mathrm{II}})$. The power $\alpha \in [1,2]$ is an empirical factor derived from mixed-mode tests for interlaminar fracture (Jiang et al., 2007). G_{IC} is mode I critical SERR. $G_{\mathrm{IIC,E}}$ is the enhanced mode II critical SERR due to TTC, as defined by:

$$G_{\mathrm{IIC,E}} = \left(\frac{\sigma_{\mathrm{II,E}}^{\max}}{\sigma_{\mathrm{II}}^{\max}}\right)^2 G_{\mathrm{IIC}} \tag{12}$$

where G_{IIC} is the un-enhanced (i.e. zero through thickness compression) mode II critical SERR. The definitions of TTC enhancement for strength and SERR, given respectively by Eq. 6 and Eq. 12, have been proved to work quite well for a wide range of fibre reinforced composites, as discussed in Refs. (Gan et al., 2013; Li et al., 2008).

Mode I and II SERRs at full failure correspond to the areas associated with the two triangles drawn in dashed blue lines in the mode I and mode II subplots in Fig. 1b. These can be equivalently expressed as $0.5\sigma_{\mathrm{I}}^{Y}\delta_{\mathrm{I}}^{\mathrm{f}}$ and $0.5\sigma_{\mathrm{II}}^{Y}\delta_{\mathrm{II}}^{\mathrm{f}}$, where the mode I and II displacement components at full failure ($\delta_{\mathrm{I}}^{\mathrm{f}}$ and $\delta_{\mathrm{II}}^{\mathrm{f}}$) can be given as $\delta_{\mathrm{m}}^{\mathrm{f}} cosI$ and $\delta_{\mathrm{m}}^{\mathrm{f}} cosII$, respectively. Thus, the overall displacement at full failure $\delta_{\mathrm{m}}^{\mathrm{f}}$ can be derived by substituting its mode I and II components into the failure criterion defined in Eq. 11. This leads to:

$$\left(\frac{0.5\sigma_{\mathrm{I}}^{Y}\delta_{\mathrm{m}}^{\mathrm{f}} cosI}{G_{\mathrm{IC}}}\right)^{\alpha} + \left(\frac{0.5\sigma_{\mathrm{II}}^{Y}\delta_{\mathrm{m}}^{\mathrm{f}} cosII}{G_{\mathrm{IIC,E}}}\right)^{\alpha} = 1 \tag{13}$$

The damage variable definition in Eq. 8 corresponds to the ratio of the damaged area to the total area of a cohesive element (Jiang et al., 2007; Turon et al., 2007). For the convenience of calculating tractions in the stiffness degradation stage, particularly when fatigue comes into play, the damage variable needs to be converted to a stiffness-degradation measure ${}^{\mathrm{K}}D_{\mathrm{s}}$. Use of the stiffness-based damage variable also better reflects the loading and unloading relationship between the twin elements. For the more deformed element, the conversion can be achieved by (Jiang et al., 2007; Turon et al., 2007):

$$ {}^{\mathrm{K}}D_{\mathrm{s}} = 1 - (1 - D_{\mathrm{s}})\frac{\delta_{\mathrm{m}}^{0}}{\delta_{\mathrm{m}}} \tag{14} $$

For the less deformed twin element, the damage variable conversion requires the aid of a reference static bilinear curve (Zhang et al., 2020a). The latter is constructed based on the displacement ratios $cosI$ and $cosII$ associated with the element and by assuming that the constitutive response of the less deformed twin element follows an unloading from the reference curve with no change on mode mixity. Fig. 3 demonstrates the idea through two twin elements in the load build-up stage of a partially reversed mode II case. Specifically, the reference static bilinear curve is described by the 'failure initiation' displacement $\delta_{\mathrm{m}}^{0,\mathrm{Ref}}$, the 'maximum strength' $\sigma_{\mathrm{m}}^{\mathrm{max,Ref}}$ and the 'full-failure' displacement $\delta_{\mathrm{m}}^{\mathrm{f,Ref}}$. $\delta_{\mathrm{m}}^{0,\mathrm{Ref}}$ is derived by the failure initiation criterion in Eq. 9, and $\delta_{\mathrm{m}}^{\mathrm{f,Ref}}$ is derived by the full failure criterion in Eq. 13, based on the displacement ratios $cosI$ and $cosII$ of the element. The reference displacement $\delta_{\mathrm{m}}^{\mathrm{Ref}}$ can then be derived by replacing δ_{m}^{0} and $\delta_{\mathrm{m}}^{\mathrm{f}}$ with $\delta_{\mathrm{m}}^{0,\mathrm{Ref}}$ and $\delta_{\mathrm{m}}^{\mathrm{f,Ref}}$ in Eq. 8, respectively. Finally, $\delta_{\mathrm{m}}^{\mathrm{Ref}}$ and $\delta_{\mathrm{m}}^{0,\mathrm{Ref}}$ are substituted into Eq. 14 to separately replace δ_{m}^{0} and δ_{m} to complete the damage variable conversion for the less deformed element.

Thus, mode I and II tractions in the stiffness degradation region can be determined for both elements by the stiffness-based damage variable:

$$ \sigma_{\mathrm{I}} = \left(1 - {}^{\mathrm{K}}D_{\mathrm{s}}\right)K_{\mathrm{I}}\delta_{\mathrm{I}}; \qquad \sigma_{\mathrm{II}} = \left(1 - {}^{\mathrm{K}}D_{\mathrm{s}}\right)K_{\mathrm{II}}\delta_{\mathrm{II}} \tag{15} $$

The shear stress components of the elements are decomposed based on the sliding displacement ratios by:

$$ \sigma_{13} = \sigma_{\mathrm{II}}\delta_{\mathrm{I3}}/\delta_{\mathrm{II}}; \qquad \sigma_{23} = \sigma_{\mathrm{II}}\delta_{23}/\delta_{\mathrm{II}} \tag{16} $$

The normal stress of the elements is assigned the mode I traction when crack is opening, otherwise, the well-known penalty contact algorithm is defined for the normal stress to inhibit penetration (Hallquist et al., 1985). These are mathematically expressed by:

$$ \sigma_{11} = \begin{cases} \sigma_{\mathrm{I}}; & \delta_{\mathrm{I}} > 0 \\ K_{\mathrm{I}}\delta_{\mathrm{I}}; & \delta_{\mathrm{I}} < 0 \end{cases} \tag{17} $$

2.2.2. Fatigue cohesive formulation

A fatigue cohesive zone may span over multiple elements, although it is generally shorter than a static cohesive zone (Allegri, 2020; Harper and Hallett, 2010). The crack-tip tracking algorithm developed in (Kawashita and Hallett, 2012) is used here. It assumes that only the crack-tip cohesive element in a cohesive zone is degraded following a fatigue cohesive formulation, whilst the remaining elements in the process zone respond according to a static cohesive formulation.

One major difference of the fatigue cohesive law presented here compared to the existing ones (Bak et al., 2016; Carreras et al., 2019b; de Moura and Gonçalves, 2014; Harper and Hallett, 2010; Kawashita and Hallett, 2012; Raimondo and Bisagni, 2020; Tao et al., 2018; Turon et al., 2007; Zhang et al., 2020a) is that the fatigue delamination propagation rate ($\mathrm{d}a/\mathrm{d}N$) is estimated by a single-hidden-layer ANN rather than by a variant of the classical Paris law.

ANN inputs

As mentioned before and illustrated in Fig. 2, the ANN used here is a single-hidden-layer feedforward network with M hidden neurons. It requires prescribing three non-dimensional parameters, χ_{f}, χ_{s} and Z in the input layer. The derivation process of these inputs is detailed in Ref. (Allegri, 2018), and emphasis is here placed on the expressions and physical interpretations of these parameters for the sake of completeness. The first two ANN inputs, χ_{f} and χ_{s}, represent the contributions of cyclic loading and static loading to the crack growth rate, respectively. They are expressed as follows (Allegri, 2018):

$$\chi_{\mathrm{f}} = \frac{\Delta\sqrt{G} - \Delta\sqrt{G_{\mathrm{th}}}}{\sqrt{G_{\mathrm{C}}}}; \qquad \chi_{\mathrm{s}} = 1 - \frac{\sqrt{G_{\max}}}{\sqrt{G_{\mathrm{C}}}} \tag{18}$$

where $\Delta\sqrt{G}$ (i.e. $\sqrt{G_{\max}} - \beta\sqrt{G_{\min}}$), instead of ΔG (i.e. $G_{\max} - \beta G_{\min}$), is employed in the cyclic loading driving input χ_{f}; the coefficient β equals -1 for a case with mode II load

reversal, or 1 for a case without load reversal. $\Delta\sqrt{G}$ obeys the principle of similitude and the rules of linear elastic superposition, while ΔG does not (Rans et al., 2011). This is because, according to linear elastic fracture mechanics (LEFM), $\Delta\sqrt{G}$ is proportional to $(P_{\max} - P_{\min})$, while ΔG is proportional to $\left({P_{\max}}^2 - {P_{\min}}^2\right)$, i.e. $(P_{\max} + P_{\min}) \cdot (P_{\max} - P_{\min})$. Hence, ΔG is dependent on both the cyclic loading and the monotonic loading, which makes it difficult to distinguish between the effects of these two loading types on crack growth. On the other hand, $\Delta\sqrt{G}$ is dependent only on the amplitude of the load cycle, while $G_{\max}$ is dependent only on the peak load, i.e. the monotonic loading component. Therefore, these two parameters are separately included in the fatigue driving input (χ_{f}) and the static damage driving input (χ_{s}) of the ANN. $\Delta\sqrt{G_{\mathrm{th}}}$ denotes the $\Delta\sqrt{G}$ threshold below which there is negligible crack growth. $G_{\max}$ and $G_{\min}$ represent the maximum and minimum SERRs over a cycle, and they can be evaluated by comparing the SERR values of the twin cohesive elements as follows:

$$G_{\max} = \max\left({}^1G,\ {}^2G\right);\quad G_{\min} = \min\left({}^1G,\ {}^2G\right) \tag{19}$$

Eq. (19) is based on a simple superposition rule, as G is the sum of mode I SERR (G_{I}) and mode II SERR (G_{II}), which are separately computed as the integral of tractions multiplied by separations for individual mode traction vs. response curves, given in Eq. 20. As an example, the SERR values of two twin elements are indicated by ${}^1G$ and ${}^2G$ in Fig. 3 for the static stage and Fig. 4 for the fatigue stage.

$$G_{\mathrm{I}} = \int \sigma_{\mathrm{I}} d\delta_{\mathrm{I}};\qquad G_{\mathrm{II}} = \int \sigma_{\mathrm{II}} d\delta_{\mathrm{II}} \tag{20}$$

G_{C} denotes the critical SERR (i.e. the fracture toughness) under a prescribed mode mixity. In Ref. (Zhang et al., 2020a), G_{C} is defined as the sum of the mode I and II SERRs at full failure, which are estimated based on the element deformation ($cosI$ and $cosII$). These two SERR components correspond to the areas associated with the two triangles drawn with blue

lines in the mode I and mode II subplots in Fig. 1b; the resulting fracture toughness is therefore given by:

$$G_{\mathrm{C}} = \frac{1}{2}\sigma_{\mathrm{I}}^{Y}\delta_{\mathrm{I}}^{f} + \frac{1}{2}\sigma_{\mathrm{II}}^{Y}\delta_{\mathrm{II}}^{f} \tag{21}$$

Apart from the element-deformation-based approach, an alternative way of determining G_{C} is based on the mode mixity $\emptyset$ via the power-law failure criterion in Eq. 11, and it is expressed by Eq. 22. These two approaches of defining G_{C} will be further discussed later.

$$G_{\mathrm{C}} = \frac{G_{\mathrm{IC}}G_{\mathrm{IIC,E}}}{\left\{\left[G_{\mathrm{IIC,E}}(1-\emptyset)\right]^{\alpha} + G_{\mathrm{I}}\emptyset^{\alpha}\right\}^{\frac{1}{\alpha}}} \tag{22}$$

To account for the possible mode mixity variation during one cycle, the averaged G_{C} value of the twin cohesive elements is here used for the ANN inputs in Eq. 18.

The third input (Z) required by the ANN describes the brittleness of a material. In combination with the damage initiation criterion in Eq. 5 and the full failure criterion in Eq. 11, the brittleness parameter for a given mode mixity is given by Eq. 23, based on the assumption made in Refs. (Allegri et al., 2013; Andersons et al., 2001; Mandell and Meier, 1975) about the stress field at a crack tip. A constant stress zone of length l_{c} is assumed to exist immediately ahead of the crack tip, and the stress distribution beyond the constant stress zone follows the classical linear elastic fracture mechanics, i.e. $\sqrt{G_{\mathrm{i}}/(2\pi\alpha_i r)}$, where α is a normalised material stiffness, r is the distance from the crack tip, and i indicates mode I or II.

$$Z = \frac{1}{2\pi\sqrt{\sigma_{\mathrm{I}}^{\max 2}\emptyset + \sigma_{\mathrm{II}}^{\max 2}(1-\emptyset)}}\left[\frac{\sigma_{\mathrm{II}}^{\max}(1-\emptyset)}{\alpha_{\mathrm{I}}\sigma_{\mathrm{I}}^{\max}} + \frac{\sigma_{\mathrm{I}}^{\max}\emptyset}{\alpha_{\mathrm{II}}\sigma_{\mathrm{II}}^{\max}}\right] \tag{23}$$

ANN formulation

For the convenience of data processing, the three inputs (χ_{f}, χ_{s} and Z) and the output (Y) of the ANN were all linearly rescaled in the [0,1] range prior to training the ANN (Allegri, 2018). The scaling that relates the ANN output and the crack propagation rate is defined by (Allegri, 2018):

$$Y = \frac{2}{\pi}\tan^{-1}\left[\log_{10}\frac{1}{l_c}\frac{da}{dN}\right] \tag{24}$$

The single-hidden-layer ANN output is expressed as:

$$Y = \sum_{i=1}^{M} c_i \psi(w_i^1 \chi_f + w_i^2 \chi_s + w_i^3 Z + \theta_j) \tag{25}$$

where w_i^1, w_i^2, w_i^3 are the random inner weights between the input layer and the hidden layer (see Fig. 2); θ_j are the random thresholds for the activation function ψ; c_i represents the outer weights between the hidden layer and the output layer. The activation function considered here is the classical logistic function:

$$\psi = \frac{1}{1+e^{-x}},\ x \in \mathbb{R} \tag{26}$$

The outer weights are determined by minimising the sum (S) of the squares of the residuals between the Y values given by experimental measurements and the ANN. Mathematically, the sum S is expressed by:

$$S = \sum_{i=0}^{K}\left[Y^i - \sum_{j=1}^{M} c_j \psi\left(w_j^1 \chi_f^i + w_j^2 \chi_s^i + w_j^3 Z^i + b_j\right)\right]^2 \tag{27}$$

where Y^i is the value of Y derived by Eq. 24 and corresponding to the i-th experimentally measured $\mathrm{d}a/\mathrm{d}N$.

Fatigue damage variable

With the fatigue crack propagation rate output from the ANN by Eqs. 24-25, the number of cycles that the twin crack-tip elements can sustain before full failure, i.e. ΔN_e, is provided by:

$$\Delta N_e = \frac{\mathrm{d}N}{\mathrm{d}a} l_f \tag{28}$$

where l_f is the fatigue characteristic length, which represents the length of the crack-tip element in the crack growth direction. To consider the possible variation of crack growth direction within one cycle, Eq. 28 employs the averaged l_f value of the two twin elements, i.e.

$$l_{\mathrm{f}} = ({}^{1}l_{\mathrm{f}} + {}^{2}l_{\mathrm{f}})/2 \tag{29}$$

where ${}^{1}l_{\mathrm{f}}$ and ${}^{2}l_{\mathrm{f}}$ are the characteristic lengths associated to the individual elements. According to Eqs. 24, 25, 28 and 29, the twin elements have the same fatigue life (ΔN_{e}). This physically makes sense since they are used to describe the same segment of an interface.

It is then required to know the fatigue damage rate ($\mathrm{d}D_{\mathrm{f}}/\mathrm{d}N$) for estimating the fatigue damage variable. At a point when the crack-tip twin elements have the static damage variable D_{s}, the elements need to accumulate an additional fatigue damage equal to $(1 - D_{\mathrm{s}})$ for full failure. The number of cycles that the twin elements can sustain at this point is ΔN_{e} given by Eq. 28. Thus, the fatigue damage per cycle $\mathrm{d}D_{\mathrm{f}}/\mathrm{d}N$ can be expressed by Eq. 30 (Kawashita and Hallett, 2012). The twin elements share the same fatigue damage rate since they have the same ΔN_{e} and D_{s}.

$$\frac{\mathrm{d}D_{\mathrm{f}}}{\mathrm{d}N} = \frac{1 - D_{\mathrm{s}}}{\Delta N_{\mathrm{e}}} \tag{30}$$

In an explicit FE framework, the fatigue damage variable is updated by (Kawashita and Hallett, 2012):

$${}^{t+\Delta t}D_{\mathrm{f}} = {}^{t}D_{\mathrm{f}} + \frac{\mathrm{d}D_{\mathrm{f}}}{\mathrm{d}N} f_{\mathrm{N}} \Delta t \tag{31}$$

where f_{N} is the numerical fatigue frequency and Δt is the time increment. According to Eq. 31, the twin elements have the same fatigue damage variable D_{f} only if they share the same value of f_{N} and the same Δt. This requirement, which is straightforward to meet in an FE programme, ensures the local synchronisation between two twin cohesive elements regarding the interface fatigue damage D_{f}. D_{f} is also an interface-area-based damage indicator, akin to the static damage variable D_{s} as defined in Eq. 8. The total damage variable D_{t}, which is equal to the sum of D_{s} and D_{f}, needs to be transformed to an interface-stiffness-based damage variable by Eq. 14, in order to evaluate the corresponding tractions in the fatigue degradation stage via Eq. 15. The transformation requires again the reference bilinear static curve that

was previously introduced for the less deformed element during the static stage. However, in the fatigue stage, a reference curve is needed for the twin cohesive elements. Fig. 4 presents an illustration of the reference static bilinear curves of two twin cohesive elements in the fatigue stage of a partially reversed fatigue case.

2.3. Finite element implementation

The cohesive formulation can be in principle implemented in any commercial FE package which supports a user-defined interface material. In this study, the cohesive formulation was implemented in a user-defined material subroutine (VUMAT) for the explicit FE package Abaqus/Explicit 6.14 in combination with four integration points (IPs) cohesive elements (COH3D8 element in Abaqus). Fig. 5 summarises the workflow of implementing the cohesive formulation in Abaqus.

The 4-IP cohesive element used in this study has its four integration points on the corners of its mid plane, as shown in Fig. 6. The 3-axis of each IP follows the normal direction of the mid-plane at the IP location, and the 1-2 plane is orthogonal to the 3-axis. The 4-IP cohesive element has been found to be more robust and give higher accuracy than a single-integration (1-IP) cohesive element in many cases, especially when high shear deformation occurs. Considering that the deformation at one IP in a 4-IP cohesive element may influence in a non-physical fashion the adjacent IPs as a result of the element linear geometry, the model implementation for 4-IP cohesive elements is here based on the averaging strategy presented in Ref. (Tao et al., 2018). As shown in Fig. 5, the critical SERRs G_c and mode mixities $\emptyset$ of all IPs of a pair of cohesive elements are averaged, and the SERRs of the 4 IPs in each cohesive element are averaged to compute $\Delta\sqrt{G}$ and $G_{\max}$. All these variables are then input into the ANN to calculate the fatigue crack propagation rate. For a 4-IP cohesive element, the characteristic length is here estimated as the length of a line that cuts the element mid-plane in the direction of the G/G_C gradient at the element centroid. This approach is similar to the

energy-based approaches used in Refs. (Carreras et al., 2019a, 2018). The G/G_C gradient is simply evaluated by the combination of linear shape functions and the G/G_C values associated with the four IPs of a 4-IP cohesive element. As mentioned previously in Eq. 29, the averaging scheme is also applied to the characteristic length l_f for the twin elements, which is then plugged into Eq. 28 to assess the fatigue life.

3. Model verification

3.1. Model generation

The modelling technique is here verified considering virtual tests performed on the edge-crack cantilever shown in Fig. 7a, where the coupon dimensions are also indicated. The cantilever consists of a unidirectional carbon-epoxy T800H/#3631 laminate. The reason why we consider this specific composite material is that, to the authors' knowledge, it is the only one for which experimental fatigue delamination growth data for the full mode mixity range, as well as reversed loading, are available in the literature (Tanaka et al., 1999, 1995; Tanaka and Tanaka, 1997). It is worth pointing out that the verification process entails comparing the model prediction to analytical solutions. The latter were obtained by plugging the analytical expressions of the ERR range and peak value into the ANN and calculating the corresponding delamination growth rate. This verification process is meant to assess if the coupling of the ANN approach with the FE CZM model is robust, particularly in the case of reversed loading. The coupon comprises a 50 mm long pre-crack. The latter is determined by the requirement that the ratio of the pre-crack length to the overall specimen length needs to be larger than 0.55 to achieve stable crack growth in a mode II ELS test (International Standard ISO/DIS 15114, 2012). The laminate is loaded by a pair of moments (M, χM) respectively applied on bottom and top arms at the crack end in Fig. 7a. Employing Euler–Bernoulli beam theory (EBT) and LEFM, Williams (Williams, 1988) established closed form

expressions relating moment ratio χ and the mode mixity $\emptyset$, as well as the resulting mode I and mode II SERR components under a given mode mixity. When the moment ratio is kept constant, the mode ratio and the SERR components are all independent of the crack length, which represents an ideal scenario for validating fatigue models (Harper and Hallett, 2010; Robinson et al., 2005; Turon et al., 2007). The relation between the moment ratio χ and the mode mixity $\emptyset$ is given by:

$$\chi = \frac{\sqrt{4\emptyset}-\sqrt{3(1-\emptyset)}}{\sqrt{4\emptyset}+\sqrt{3(1-\emptyset)}}, \quad 0 \le \emptyset \le 1, \ -1 \le \chi \le 1 \tag{32}$$

For a mode I DCB test ($\emptyset$=0), χ in Eq. (32) equals -1, thus a pair of equal and opposite moments are applied on the top and lower arms. For a mode II ELS test ($\emptyset$=1), χ equals 1, thus a pair of equal and same-direction moments are applied. In a mixed-mode case, χ falls in the (-1, 1) range. The SERR components for mode I and mode II are given by Eq. 33, where B, E and I indicate the width, the longitudinal flexural modulus and the second moment of area of the arm, respectively.

$$G_{\mathrm{I}} = \frac{(1-\chi)^2 M^2}{4BEI}; \qquad G_{\mathrm{II}} = \frac{3(1+\chi)^2 M^2}{16BEI} \tag{33}$$

According to the modelling strategy introduced in Section 2.1, the laminate was described by two twin cohesive models. For the model representing the laminate at the peak load, the lower and upper arms were respectively loaded with the moments $M_{\max}$ and $\chi M_{\max}$ at the cracked end for 5 seconds of simulation time, then both held at a constant load for 1 second before entering the fatigue step. Regarding the sister model representing the laminate under the trough load, the lower and top arms were respectively loaded with the moments $M_{\min}$ and $\chi M_{\min}$ at the cracked end, again for 5 seconds followed by a 1 second hold time before entering fatigue step. The global load ratio is $R = M_{\min}/M_{\max}$. As an example, Fig. 7b shows the boundary conditions for the 0.64 MMB case with $R = 0.2$ in the fatigue step. Four load envelopes were required for these models, respectively corresponding to $M_{\max}$,

$\chi M_{\max}$, $M_{\min}$ and $\chi M_{\min}$. The two envelopes of $\chi M_{\max}$ and $\chi M_{\min}$ are built on the baseline ones corresponding to $M_{\max}$ and $M_{\min}$ via the moment ratio χ.

More in detail, a 0.5 mm wide slice mesh was used to model the laminate under generalised plane strain boundary conditions, which are applied to both sides of the slice model. This entails assuming that the crack front is straight across the laminate width (Mohamed et al., 2018). Each arm of the laminate was discretised by regular 1-IP hexahedral elements (C3D8R in Abaqus), using one element in the width direction and three elements in the thickness direction. To avoid hourglass deformation (i.e. zero energy modes) in the reduced-integration elements, a linear combination of stiffness and viscous hourglass control was used (Flanagan and Belytschko, 1981); this option has been proved to be able to suppress zero energy modes and have negligible influence on the numerical results. One layer of 0.01 mm thick and 0.02 mm long 4-IP cohesive elements (COH3D8) was inserted between the top and bottom arms to simulate delamination. For convenience, all the twin cohesive elements were numbered so that each pair of them had an interval of 50000, e.g. element 1 and element 50001 at the initial crack tips. The mesh sensitivity of a fatigue CZM is influenced by the loading severity. A low-severity fatigue model has a smaller cohesive zone length than a high-severity fatigue model, thus the former requires a finer mesh than the latter in order to achieve a fully developed cohesive zone, as it was demonstrated by a cut-ply model in Ref. (Zhang et al., 2020a). Thus, using a mesh with 0.02 mm element length in the propagation direction allows achieving numerical convergence at all severities, including the ones close to near-threshold 10^{-6} mm/cycle regime, as presented below. The material properties used for all the models here are listed in Table 1 (Chou et al., 1995; Gan et al., 2013; Tanaka et al., 1999).

ANN training

The ANN as illustrated in Fig. 2 was trained according to the "extreme learning" paradigm

(Allegri, 2018) and validated before it was plugged into the CZM framework to run these single-interface benchmark models. Note that the ANN is used here to replace the classical Paris law and thus to evaluate delamination growth rate under various stress ratios and mode mixity values. The rationale for this choice is that a semi-empirical power law of the Paris type able to span the entire mode-mixity and stress ratio ranges (including reversed loading) is yet to be found. It is worth pointing out that it has been rigorously demonstrated that single-hidden-layer ANN possess a "universal approximation capability" (Huang et al., 2011), i.e. given an arbitrary function $f(x_1, x_2, \dots x_N)$ defined in a compact subset of R^N space, a single-hidden-layer ANN is able to represent the function within an arbitrary small tolerance for a sufficiently large (but finite) number of neurons in the hidden layer. The universal approximation capability implies that there is no doubt that the single-hidden-layer ANN can represent the delamination growth rate $\mathrm{d}a/\mathrm{d}N$, at least from a purely mathematical point of view. Note that, in general, ANNs with multiple hidden layers are not universal approximants.

DCB/ELS/MMB tests are widely employed to experimentally characterise delamination growth rates for various stress ratios and mode mixity values. The ANN employed here was trained and validated using DCB/ELS/MMB experimental data that are presented in Refs. (Tanaka et al., 1999, 1995; Tanaka and Tanaka, 1997) for the carbon-epoxy system T800H/#3631. In more detail, training of the ANN was performed by using 60% of the experimental data (including mode I results at 0.2 and 0.5 *R* ratios, 0.42 MMB results and mode II results for -1, 0.2 and 0.6 *R* ratios), while the remaining 40% of experimental data (0.64 MMB results, 0.84 MMB results and mode II results for -0.5 and 0.5 *R* ratios) were used for validation. This division of the input data in sets provided sufficient information both for the ANN to learn the effects of mode mixity and stress ratio and to test (i.e. validate) the ANN on combinations of ERR, stress ratio and mode-mixity that were not included in the

training set. As a matter of fact, given the "universal approximant" property of the single-hidden-layer ANN considered here, we are interpolating a subset of experimental data within a region which is bounded by: 1) threshold (no growth) and static fracture in terms of delamination growth rates; 2) mode I and mode II behaviour; 3) fully reversed (R = -1) and static loading (R = +1).

The inner weights and the activation thresholds were sampled from a standard Gaussian distribution function with zero mean and unit standard deviation. The outer weights of the ANN were derived by using the function LSQLIN in MATLAB 2018a to solve the least-square problem in Eq. 27. The number of neurons was progressively increased from 10 to 1000, and the root mean square error was evaluated from Eq. 27 by $\sqrt{C/K}$. By further pruning the outer weights that have an absolute value less than 10^{-6} of the maximum of the outer weights, only 18 neurons were needed for the ANN to give predictions with a 3% error on the validation data set. This demonstrates that the ANN has an actual predictive capability beyond mere interpolation. The inner and outer weights as well as the activation thresholds of the ANN are given in Table 2.

3.2. Model results

All the FE models were evaluated by incrementally reducing the numerical fatigue frequency f_N until the predicted crack propagation rate converged. Figs. 8-11 provide a comparison of the analytical solutions and FE predictions regarding the fatigue crack growth rates for mode I DCB, mode II ELS without reversal, mode II ELS with reversal and, finally, MMB tests. The insets in these figures show the twin models at the start of fatigue stage (i.e. the end of the load-holding stage) for the highest load severity that was computed for each case. Analytical solutions were obtained by EBT and LEFM (Eqs. 32-33), in combination with the ANN output (Eqs. 18 and 23-25). The analytical solutions have been validated against experimental data in Ref. (Allegri, 2018). The $\Delta\sqrt{G}$ and $\mathrm{d}a/\mathrm{d}N$ ranges of the

analytical solutions were determined by the experimental data that had been employed for the ANN training, with a threshold fatigue crack propagation rate of 10^{-6} mm/cycle (Allegri, 2018).

The crack propagation rates predicted by the FE models were computed by counting the number of cycles elapsed over a crack length. As mentioned in Section 2.3, the ERRs of the 4 IPs belonging to each cohesive element were averaged to achieve the $\Delta\sqrt{G}$ value for the ANN inputs (see Fig. 5), thus the element-level averaged ERRs were used to plot the $\Delta\sqrt{G}$ values in Figs. 8-11. Furthermore, the SERR value varies in the fatigue degradation region of the cohesive law (recall Fig. 4), thus $\Delta\sqrt{G}$ also varies during the fatigue degradation process. The averaged $\Delta\sqrt{G}$ value between the start of fatigue degradation and full failure was used to indicate the $\Delta\sqrt{G}$ given in the FE plots. An alternative way of obtaining the averaged $\Delta\sqrt{G}$ is to first compute the averaged SERR value between the start of fatigue degradation and full failure for each twin element and then calculate $\Delta\sqrt{G}$ by the averaged ERR values. Nonetheless, a comparison of these two approaches for the models presented here showed negligible difference.

Mode I and mode II without reversal

The Mode I FE results in Fig. 8 were achieved by loading the twin cohesive models under the moment pairs derived from Eqs. 32-33 at 0.31, 0.37, 0.42 and 0.53 $G_{\max}/G_{\mathrm{C}}$ ratios for the R = 0.2 DCB case, and 0.45, 0.52, 0.57 and 0.61 severities for the R = 0.5 DCB case, respectively. There exists a slight mismatch between the FE and analytical $\Delta\sqrt{G}$ values, mainly due to the aforementioned $\Delta\sqrt{G}$ variation occurring during the fatigue degradation process. A further refined mesh could help reduce the $\Delta\sqrt{G}$ variation, but it will significantly increase the computational cost. However, as shown in Fig. 8, a good agreement is achieved between FE models and analytical formulas regarding mode I fatigue crack growth rates.

Fig. 9 presents the analytical solutions and FE predictions for mode II non-reversed

fatigue. FE results were computed corresponding to 0.15, 0.25, 0.35 and 0.45 $G_{\max}/G_{\mathrm{C}}$ ratios for the R = 0.2 ELS case, and 0.35, 0.45, 0.55 and 0.65 severities for the R = 0.5 ELS case. Again, an excellent agreement between FE predicted and analytical $\mathrm{d}a/\mathrm{d}N$ values is achieved for the mode II cases without load reversal.

Reversed mode II

As previously mentioned, one of the main objectives of this study is expanding the prediction capability of the twin-model-based DLE modelling strategy to cover the reversed mode II regime, with the aid of the ANN-based description of delamination growth rates. For the reversed mode II models, FE results were computed corresponding to 0.08, 0.13, 0.18 and 0.23 $G_{\max}/G_{\mathrm{C}}$ ratios for the R = -0.5 case, and 0.05, 0.08, 0.11 and 0.14 $G_{\max}/G_{\mathrm{C}}$ ratios for the R = -1 case. As shown in Fig. 10, the numerical models also correlate very well with the analytical results for the reversed load cases.

The effects of the numerical fatigue frequency are here illustrated considering the mode II reversed-load models. As it is exemplified by the 5% $G_{\max}/G_{\mathrm{C}}$ ratio and $R = -1$ model in Fig. 12, with decreasing the numerical fatigue frequency the traction versus displacement response of twin cohesive elements tends to be linear in the fatigue degradation stage. This is consistent with the finding of Ref. (Zhang et al., 2020a) by a central cut-ply laminate model where there was not load reversal. Thus, the linear traction versus displacement relation can be used as the criterion to judge whether the numerical fatigue frequency is small enough for models to converge when the fatigue cohesive law presented in Section 2.2.2 is used. In Fig. 12, the 5% $G_{\max}/G_{\mathrm{C}}$ ratio and $R = -1$ model converged at 1×10^5 Hz. In addition, at the converged frequency the crack growth in the simulations complied with the self-similarity principle. On the other hand, at a higher frequency the element pairs had different traction versus displacement responses and, globally, the crack growth rate also varied with the crack length. The plots in Fig. 12 were extracted from one of the two leading integration points of

the elements (i.e. the "forward" IPs in the crack growth direction), but there was very minor difference amongst the four IPs because of the fine mesh employed in the simulations.

As mentioned in Section 2.2.2, the parameter β used in the $\Delta\sqrt{G}$ formula, i.e. $\sqrt{G_{\max}} - \beta\sqrt{G_{\min}}$ differentiates between load reversal case (β = -1) and non-reversal case (β = 1). This was computed on the fly by combining the mode mixity ϕ with a dot product and the sign function (sgn):

$$\beta = \begin{cases} 1; & \phi < 0.99 \\ sgn\left({}^{1}\delta_{13}\, {}^{2}\delta_{13} + {}^{1}\delta_{23}\, {}^{2}\delta_{23}\right); & \phi \geq 0.99 \end{cases} \quad (34)$$

where (${}^{1}\delta_{13}$, ${}^{1}\delta_{23}$) and (${}^{2}\delta_{13}$, ${}^{2}\delta_{23}$) indicate the shear displacement components of two twin elements. A close-to-one value of 0.99 was used here to discriminate between mode II and mixed-mode/mode I. The simple approach worked well for all the models presented here. The combination of a dot product and the sign function was employed to estimate β in mode II for removing the influence of potential numerical instabilities. The ideal displacement vectors of two twin elements in mode II should have a zero value for δ_{23}, however, due to numerical truncation errors, δ_{23} always had a small and non-zero value. To confirm the robustness of the proposed approach, the β plot in Fig. 12 shows that mode II reversal was successfully recognised since the parameter β had a value of -1 throughout the whole analysis. The MMB cases with reversed mode II component will be studied in future work, as experimental results are not available for such loading scenarios.

Mixed mode

Fig. 11 presents the MMB modelling results corresponding to 0.3, 0.38, 0.55 and 0.65 $G_{\max}/G_{\mathrm{C}}$ ratios for the 0.42 mode ratio, and 0.23, 0.35, 0.49 and 0.67 severities for the 0.64 mode ratio, and finally, 0.18, 0.28, 0.41 and 0.55 severities for the 0.84 mode ratio. The FE modelling strategy also agrees well with the analytical calculations in the mixed-mode regime.

One aspect that deserves special attention for the MMB fatigue modelling is the mode mixity change, which is not in detail discussed in the literature to the best of the authors' knowledge. This is illustrated in Fig. 13 by plotting the mode ratios of the leading and trailing IPs of selected cohesive elements from the peak-load model of the 55% $G_{\max}/G_{\mathrm{C}}$ ratio and 0.84 MMB case. The mode ratio of an IP was computed on the fly from the point when the IP entered the static stiffness degradation stage of the cohesive law until full failure. The mode ratios from the trough-load model are not plotted here, because there was minor mode-ratio difference between two twin IPs in an MMB case (Zhang et al., 2020a). However, apparent mode-ratio difference existed between the leading IP and trailing IP of a cohesive element during both the static (< 5s) and cyclic (> 6s) loading stages by comparing two same-colour solid and dash curves in Fig. 13). More in detail, during the static stage (up to 5s), a cohesive zone was partially developed, and it spanned from the initial crack-tip element 1 to element 21 in the peak-load model or from element 50001 to element 50021 in the trough-load model. Each leading IP in the partially developed cohesive zone entered the stiffness degradation stage with a mode mixity much larger than the nominal value (0.84 in this case), and the mode mixity progressively decreased towards the nominal value. Also, the mode mixities of leading IPs increased along the cohesive zone. These findings related to the leading IPs correlate well with the single-IP static MMB models discussed in Ref. (Harper et al., 2012). Differently, the trailing IP at the initial crack tip entered the stiffness degradation stage with a mode ratio much lower than the nominal value, and then approached the nominal value as the simulation advanced. In the static loading stage, the mode-mixity difference between the leading IP and trailing IP of a cohesive element decreased with loading.

There was apparently negligible mode-ratio change during the load-holding stage (from 5s to 6s). Once the modelling entered the fatigue stage from 6s, the initial crack-tip twin elements 1 and 50001 started to accumulate fatigue damage, and other non-crack-tip elements

in the cohesive zone continued to accumulate static damage as the crack-tip tracking algorithm was used (Kawashita and Hallett, 2012). When the initial crack-tip elements were fully failed due to fatigue, the next twin elements (elements 2 and 50002) became the new crack tip and started to be fatigue degraded. Simultaneously, the cohesive zone was extended to elements 22 and 50022, while the next twin elements (elements 23 and 50023) were still in the elastic region. These sequences were repeated during the fatigue loading stage, resulting in a fully developed cohesive zone that moved in the crack growth direction with the number of elapsed fatigue cycles. Self-similar fatigue crack growth was achieved from the point when the twin elements 22 and 50022 became crack tips, which is confirmed by observing in Fig.13b that the elements 22, 26 and 51 have the same shape of mode ratio plot. This is because that all the elements placed after elements 22 and 50022 were entirely loaded during the fatigue stage (after 6s), whilst the preceding elements (i.e. elements 1 to 21 or elements 50001 to 50022) experienced both the static stage (up to 5s) and fatigue stage (after 6s).

In the fatigue stage (from 6s), the mode ratio of each cohesive IP showed a clearly decreasing trend throughout the stiffness degradation stage of the cohesive law, which includes the static degradation stage when the IP was not a crack tip and the fatigue degradation stage when the IP became a crack-tip (recall Fig. 4). It is important to observe that most of the mode ratio change at an IP occurred during the static stiffness degradation stage, and there was only a minor mode-mixity change during the fatigue stiffness degradation stage of the cohesive law, as it can be confirmed by observing the initial crack-tip IP plots in Fig. 13b. Fig. 14 shows that the mode ratio at full failure gradually increased with the distance from the initial crack tip and it plateaued once self-similar crack growth was achieved starting from elements 22 and 50022. This was true for both the leading and trailing IPs. The averaged mode ratio of trailing and leading IPs at full failure reached the nominal mode ratio in the self-similar crack growth region. This confirms that the averaging method

used for dealing with the variable mode mixity in the proposed modelling framework is sound (see Fig. 5).

4. A tapered laminate under combined static tension and cyclic bending

In the single-interface benchmark models presented in Section 3, the local energy release rate ratio (R_{G}) can be directly calculated from the global *R* ratio using Eq. 35 (Zhang et al., 2020a).

$$R_{\mathrm{G}} = \frac{G_{\min}}{G_{\max}} = R^2 \tag{35}$$

This section presents a numerical example where the local *G* ratio cannot be calculated a priori from the global *R* ratio, because of the non-proportional nature of the applied load. The example consists of a symmetrically tapered laminate, which is subjected to combined static tension and cyclic bending, as it is illustrated in Fig. 15a. This loading scenario is representative of "in service" conditions in components such as the roots of composite wind turbine blades, which usually experiences static tension due to centrifugal force and cyclic bending due to aerodynamically induced vibrations. Fig. 15a also includes the overall dimensions of the tapered laminate. The laminate was designed based on a previous study (Zhang et al., 2020b), which investigated the tensile failure mechanisms of composite laminates due to the presence of ply drop-offs. The laminate has the symmetric stacking sequence [-45/0/45/0/-45/0/45/0/45/0/0/-45/0/45/0/-45]$_{\mathrm{S}}$, where the underscores indicates dropped plies. This implies that the thickness ratio between its thick section and its thin section is 2:1. The ply drop spacing is 2 mm, thus the overall taper angle of the laminate is 8.1°, a fairly modest value. The ply thickness is 0.25 mm.

4.1. Finite element mesh

Due to symmetry, only half of the laminate needs to be considered in the FE modelling. To save computational cost, a 0.25 mm wide slice mesh was employed to describe the

laminate in combination with a generalised plane strain boundary condition applied to both side surfaces of the slice model (Kawashita and Hallett, 2012; Zhang et al., 2020a). The FE model was built using the previously developed high-fidelity meshing tool (Kawashita et al., 2011; Zhang et al., 2020b). Different from the previous study, where a physical IM7/8552 specimen was scanned to output the actual ply drop locations into the meshing tool, here nominal ply drop locations were assumed in the meshing tool since a virtual T800H/#3613 laminate is studied here, with no physical specimen available for measurements. This means that the FE model had a symmetric distribution of ply drop locations relative to its thickness mid-plane. Each ply and each resin pocket were both described by one layer of 1-IP hexahedral elements (C3D8R). The element size along the laminate length was 0.1 mm in the tapered section and gradually increased towards both ends of the model. 0.01 mm thick cohesive elements were inserted between two adjacent plies, and between a resin pocket and its two neighbouring plies. Fig. 15b shows the finite element mesh of the tapered section. Ply drops in each half of the tapered section are numbered in ascending order from the thin section for ease of description. Pre-cracks were assumed to exist between the ends of each dropped ply and its adjacent resin pocket, given that resin pocket tends to fail at very low loads, often during the post-cure cooldown, thus a small gap exists between the end of each dropped ply and the corresponding resin pocket in the model, as shown in Fig. 15b. The material properties listed in Table 1 were also used for the tapered laminate modelling.

4.2. Static modelling

Static modelling was first carried out to establish a reference failure envelope for defining fatigue severities, since it is difficult to compute failure loads with analytical methods for the configuration considered here. To achieve the failure envelope, both tension and bending were synchronously applied to the laminate by following a smooth curve to minimise kinetic effects. The ratio between bending and tension was kept constant throughout a static analysis.

Tension was applied from the left-end nodes of the model. Bending was applied through the top right corner nodes of the laminate, while the left bottom nodes of the model were not allowed to move in the thickness direction of the laminate but free in other degrees of freedom, to simulate the sliding constraint shown in Fig. 15a. The static model was run several times at different bending-to-tension ratios (0, 0.0285, 0.0583, 0.0898, 0.125 and 0.157), so that the failure envelope as shown in Fig. 16 was obtained. Delamination within the tapered section is the only failure mechanism considered in this piece of study. If the bending-to-tension ratio were to be further increased, there was a risk that delamination would start from the interfaces just underneath the bending application point, rather than within the tapered section. The delamination onset took place at the ply-to-ply interfaces surrounding ply drop 1, and rapidly propagated towards the thick end of the specimen for the tension-to-bending ratios of 0, 0.0285, 0.0583, 0.0898, 0.125. On the other hand, delamination onset location shifted to ply drop 4 for the 0.157 bending-to-tension model, simply because that bending stress was more prevalent at ply drop 4 than ply drop 1.

4.3. Fatigue analysis

Referring to the modelling methodology, as summarised in Section 2.1, the tapered laminate was described by twin cohesive models for fatigue analysis. The twin models were respectively loaded to the bending peak and trough in 1s following a smooth function (Fig. 17a). The twin models were also synchronously loaded to the static tension amplitude in 1s (Fig. 17b). The bending and tension loads were held for 1s before entering the fatigue analysis stage. Two fatigue modelling cases are demonstrated here, respectively 60% tension severity and 50% bending severity, at the global stress ratio values of R = -1 and R = 0.2. The first percentage describes the severity of tensile load relative to the pure tensile strength of the laminate, while the second percentage indicates the bending severity relative to the bending strength that was determined when the 50% tension was simultaneously applied to

the laminate. The bending strength was evaluated according to the static failure envelope as achieved in Fig. 16.

Fig. 18 captures the deformation and interface failure status of the R = - 1 models at the start of the fatigue loading (2s) and after 2100 cycles of fatigue loading. Note that the damage pattern is symmetric, as it should be expected for a symmetric structure under fully reversed loading. The FE simulations show that delamination started from ply drop 4 in both the top and bottom halves of the tapered section. The interlaminar cracks continued growing towards the thick section of the laminate until unstable fracture occurred. There was also crack growth from ply drop 1, but at a much slower rate than for ply drop 4. For the R = 0.2 case, crack growth initiated from the bottom ply drop 1 and shortly afterwards the top ply drop 1 also showed crack growth.

Fig. 19a plots the local G ratio, i.e. $G_{\min}/G_{\max}$ of the top and bottom interface tips of ply drops 1 and 4 associated with the upper half of the laminate at the start of fatigue degradation. Due to symmetric set-up for the -1 R ratio case as mentioned above, ply drops 1 and 4 in the lower half of the laminate had the same local G ratios as the corresponding ones in the upper half. There was very small G ratio variation during the fatigue softening stage of these cohesive elements, and there was also very small G ratio difference amongst the integration points of these cohesive elements. It can be confirmed from Fig. 19a that due to the presence of the static tension, the local G ratio cannot be correlated with the global R ratio by Eq. 35, showing there is a large difference between two. Fig. 19b plots the local G ratios at ply drop 1 in both the upper and lower halves of the laminate for the R = 0.2 case, which further confirmed the weak correlation between the local G ratio and the global R ratio when static loading and cyclic loading are simultaneously applied to a specimen. This numerical tapered laminate case demonstrates the necessity to use the proposed twin cohesive models for a more reasonable evaluation of the local G ratio in complex, but more realistic, loading

scenarios. Moreover, the *G* ratio may vary at different locations of a laminate with multiple delaminations, as seen in Figs. 19a-b, thus it adds the appeal of using a more powerful tool to estimate the fatigue crack propagation rate for various *G* ratios. This highlights the reason why the ANN is embedded into the twin CZM modelling framework to replace the classical Paris law.

5. Discussion

Remarks on ANN

Analytical solutions are available for these single-interface cases presented in Section 3 by using the ANN, but the ANN needs to be embedded into the twin CZMs framework to predict delamination in a more complicated multi-interface application, e.g. the tapered laminate case presented in Section 4. If the modelling strategy proposed here by combing ANN and twin CZMs has been well calibrated at the single-interface level across various mode mixities and stress ratios, it would be relatively straightforward to scale it up towards more complicated applications, as it was previously demonstrated by a single load envelope model in Ref. (Tao et al., 2018), where a Paris $\mathrm{d}a/\mathrm{d}N$ formula was used. Use of the ANN is not meant to limit the application range of a fatigue CZM compared to Paris law, since they are both a way of describing fatigue growth rate. Thus, it is necessary to embed the ANN into the twin CZMs framework to expand the fatigue prediction capability. However, further verification of the modelling strategy by multi-interfaces cases such as the tapered laminate case illustrated in Section 4 needs to be addressed in a separate paper when comprehensive experimental data at both single-interface and multi-interface levels are available for a material system.

The ANN is not limited to the T800H/#3613 material. It can be trained to describe the fatigue delamination growth rate for other material systems when sufficient experimental data

are available. These also imply that the first step when using the modelling strategy presented in this study is training and validating the ANN. It is also worth highlighting that the focus of this study is on the development of the fatigue numerical methods, for which we used experimental data from "traditional" DCB/ELS/MMB (i.e. mode I/mode II/mixed-mode) tests found in literature. These tests are commonly adopted by the composites community, both in academia and industry, but with a wider study on the training of the ANN in the future, using a greater range of test types and configurations would likely be possible.

Remarks on G_C

As mentioned in Section 2.2.2, two approaches to determine G_C are used in the literature. The first is based on the element deformation (Eq. 21), whilst the second one is based on the mode mixity (Eq. 22). Since there was no mode ratio change in the DCB and ELS models, these two methods show no difference in G_C and thus the same prediction regarding fatigue crack growth rates. However, when mode ratio varies during the stiffness degradation stage, e.g. in the MMB models, these two approaches may give different G_C estimates, and thus the fatigue crack growth rates predicted when using these two approaches might be different. As shown in Fig. 11, the mode mixity based approach (Eq. 22) predicted satisfactory fatigue crack growth rate in all the MMB cases. Fig. 20 shows that in comparison with analytical solutions the element-deformation-based approach (Eq. 21) provides an overestimation of the delamination growth rate at relatively high loads, and this effect becomes more severe as the mode mixity increases. This is simply because the mode mixity based approach was also used in the analytical framework to estimate G_C (Allegri, 2018).

Another point that deserves attention regarding G_C is that it may vary during one cycle. As previously discussed, the averaged G_C value of twin cohesive elements was used in the modelling framework. The simple averaging approach gives satisfactory results for the single-interface models presented in Section 3, where there was no (DCB and ELS cases) or

minor (MMB case) G_C difference between the peak and trough models. In addition, the cut-ply models as studied in Ref. (Zhang et al., 2020a) also showed G_C variation within one cycle because of through-thickness compressive enhancement, and the simple averaging method gives good correlation with experimental measurements for the cut-ply models, however the G_C variation in the cut-ply models was also small within one cycle. Thus, the averaging approach needs to be further verified through cases where large variation in G_C occurs during one cycle in the future work.

Remarks on fatigue initiation

The modelling strategy is proposed in this study by combining the twin cohesive models and the ANN to model fatigue delamination propagation, which is dominated by the softening region of the cohesive law (recall Fig.1b). It is at least in principle feasible to extend the twin CZMs modelling strategy to the fatigue initiation regime by referring to the existing single CZM models (Iarve et al., 2017; Mukhopadhyay et al., 2018; Tao et al., 2018), which consider fatigue initiation by reducing interface strengths in the cohesive law based on *S-N* curves. Like the fatigue propagation rate, the *S-N* relation is also dependent on mode mixity and stress ratio. Thus, before extending the modelling framework to fatigue initiation regime, it is necessary to devise an analytical solution or another ANN to describe the S-N curves for various stress ratios and mode mixities. However, there are not sufficient experimental results for fatigue initiation at various stress ratios and mode mixities, even for the T800H/#3613 material system that was used for the fatigue propagation study here, which is one of the most extensively characterised in the literature. Thus, fatigue initiation modelling is not covered in this study.

6. Conclusions

This paper has presented a prediction technique for fatigue-driven delamination growth in

composites, which hinges upon embedding an artificial neural network into twin cohesive zone models. The first of such models is subjected to the peak-load envelope, while the trough-load envelope is applied to the second model. An interlaminar interface is described by two twin layers of cohesive elements, which are employed to compute local fracture mechanics variables such as SERR change, maximum SERR and mode mixity. These variables are input into a feedforward single-hidden-layer neural network. The ANN provides fatigue crack propagation rate $\mathrm{d}a/\mathrm{d}N$ to the twin cohesive elements, which are synchronously degraded by a fatigue damage variable. The modelling technique has been implemented by the combination of a user-defined material subroutine and a hexahedral solid element with four integration points in the explicit finite element package Abaqus/Explicit. It is worth mentioning that, in principle, the description of delamination growth rate based on the single-hidden-layer ANN proposed here is applicable to most fatigue cohesive zone models and FE implementations that currently make use of a Paris law expression.

The modelling strategy was calibrated and verified by several virtual fatigue testing cases, involving mode I DCB, mode II ELS and MMB without reversal, and reversed ELS tests. A satisfactory agreement between FE predicted and analytical $\mathrm{d}a/\mathrm{d}N$ values has been achieved for all the tested cases. The mode ratio change was examined for the MMB model, which has been used extensively in the literature for verifying delamination modelling techniques. It was found that mode ratio variation mainly happened during the static degradation stage of the cohesive law, whilst the mode ratio change was minor when the cohesive element was degraded due to fatigue as a crack tip. Also, the averaged mode ratio of the cohesive element over its four IPs reached the nominal mode ratio at full failure when the self-similar crack growth was established in the mixed-mode simulations. These single-interface virtual tests provide critical knowledge for scaling up the fatigue modelling technique towards multi-interface applications. A relevant example of such applications has been provided

considering a tapered laminate with multiple ply drop-offs, that promote delamination onset and fatigue-driven growth in a non-proportional loading regime.

Acknowledgements

The authors would like to acknowledge Rolls-Royce plc for the support of this research through the Composites University Technology Centre (UTC) at the University of Bristol, UK. The authors are also grateful to Innovate UK for the funding of the Aerospace Technology Institute (ATI) project "FAN Testing And STatistical Integrity CALibration" (Ref. 113190).

References

Allegri, G., 2020. A unified formulation for fatigue crack onset and growth via cohesive zone modelling. J. Mech. Phys. Solids 138, 103900.

Allegri, G., 2018. Modelling fatigue delamination growth in fibre-reinforced composites: Power-law equations or artificial neural networks? Mater. Des. 155, 59–70.

Allegri, G., Wisnom, M.R., Hallett, S.R., 2013. A new semi-empirical law for variable stress-ratio and mixed-mode fatigue delamination growth. Compos. Part A Appl. Sci. Manuf. 48, 192–200.

Amiri-Rad, A., Mashayekhi, M., van der Meer, F.P., 2017. Cohesive zone and level set method for simulation of high cycle fatigue delamination in composite materials. Compos. Struct. 160, 61–69.

Andersons, J., Hojo, M., Ochiai, S., 2001. Model of delamination propagation in brittle-matrix composites under cyclic loading. J. Reinf. Plast. Compos. 20, 431–450.

Bak, B.L. V., Sarrado, C., Turon, A., Costa, J., 2014. Delamination under fatigue loads in composite laminates: a review on the observed phenomenology and computational methods. Appl. Mech. Rev. 66.

Bak, B.L. V., Turon, A., Lindgaard, E., Lund, E., 2016. A simulation method for high-cycle fatigue-driven delamination using a cohesive zone model. Int. J. Numer. Methods Eng. 106, 163–191.

Barenblatt, G.I., 1962. The mathematical theory of equilibrium cracks in brittle fracture. Adv.

Appl. Mech. 7, 55–129.

Carreras, L., Bak, B.L.V., Turon, A., Renart, J., Lindgaard, E., 2018. Point-wise evaluation of the growth driving direction for arbitrarily shaped delamination fronts using cohesive elements. Eur. J. Mech. / A Solids 72, 464–482.

Carreras, L., Lindgaard, E., Renart, J., Bak, B.L.V., Turon, A., 2019a. An evaluation of mode-decomposed energy release rates for arbitrarily shaped delamination fronts using cohesive elements. Comput. Methods Appl. Mech. Eng. 347, 218–237.

Carreras, L., Turon, A., Bak, B.L.V., Lindgaard, E., Renart, J., Martin de la Escalera, F., Essa, Y., 2019b. A simulation method for fatigue-driven delamination in layered structures involving non-negligible fracture process zones and arbitrarily shaped crack fronts. Compos. Part A Appl. Sci. Manuf. 122, 107–119.

Chou, I., Kimpara, I., Kageyama, K., Ohsawa, I., 1995. Mode I and mode II fracture toughness measured between differently oriented plies in graphite/epoxy composites. Compos. Mater. Fatigue Fract. Vol. ASTM STP 132–151.

Dávila, C.G., 2020. From S-N to the Paris law with a new mixed-mode cohesive fatigue model for delamination in composites. Theor. Appl. Fract. Mech. 106, 102499.

De Carvalho, N.V., Mabson, G.E., Krueger, R., Deobald, L.R., 2019. A new approach to model delamination growth in fatigue using the Virtual Crack Closure Technique without re-meshing. Eng. Fract. Mech. 222, 106614.

de Moura, M.F.S.F., Gonçalves, J.P.M., 2014. Cohesive zone model for high-cycle fatigue of adhesively bonded joints under mode I loading. Int. J. Solids Struct. 51, 1123–1131.

Deobald, L.R., Mabson, G.E., Engelstad, S., Prabhakar Rao, M., Gurvich, M.R., Seneviratne, W., Perera, S., O'Brien, T.K., Murri, G., Ratcliffe, J., Dávila, C.G., De Carvalho, N. V., Krueger, R., 2017. Guidelines for VCCT-based interlaminar fatigue and progressive failure finite element analysis. Tech. Rep. NASA-TM–2017-219663.

Diniz, B. da C., Freire Júnior, R.C.S., 2020. Study of the fatigue behavior of composites using modular ANN with the incorporation of a posteriori failure probability. Int. J. Fatigue 131, 105357.

Dugdale, D.S., 1960. Yielding of steel sheets containing slits. J. Mech. Phys. Solids 8, 100–104.

El Kadi, H., 2006. Modeling the mechanical behavior of fiber-reinforced polymeric composite materials using artificial neural networks - A review. Compos. Struct. 73, 1–23.

Erpolat, S., Ashcroft, I.A., Crocombe, A.D., Abdel-Wahab, M.M., 2004. Fatigue crack

growth acceleration due to intermittent overstressing in adhesively bonded CFRP joints. Compos. Part A Appl. Sci. Manuf. 35, 1175–1183.

Flanagan, D.P., Belytschko, T., 1981. A uniform strain hexahedron and quadrilateral with orthogonal hourglass control. Int. J. Numer. Methods Eng. 17, 679–706.

Gan, K.W., Hallett, S.R., Wisnom, M.R., 2013. Measurement and modelling of interlaminar shear strength enhancement under moderate through-thickness compression. Compos. Part A Appl. Sci. Manuf. 49, 18–25.

Hallquist, J.O., Goudreau, G.L., Benson, D.J., 1985. Sliding interfaces with contact-impact in large-scale Lagrangian computations. Comput. Methods Appl. Mech. Eng. 51, 107–137.

Harper, P.W., Hallett, S.R., 2010. A fatigue degradation law for cohesive interface elements - Development and application to composite materials. Int. J. Fatigue 32, 1774–1787.

Harper, P.W., Sun, L., Hallett, S.R., 2012. A study on the influence of cohesive zone interface element strength parameters on mixed mode behaviour. Compos. Part A Appl. Sci. Manuf. 43, 722–734.

Huang, G.-B., Wang, D.H., Lan, Y., 2011. Extreme learning machines: a survey. Int. J. Mach. Learn. Cybern. 2, 107–122.

Iarve, E. V, Hoos, K., Braginsky, M., Zhou, E., Mollenhauer, D.H., 2017. Progressive failure simulation in laminated composites under fatigue loading by using discrete damage modeling. J. Compos. Mater. 51, 2143–2161.

International Standard ISO/DIS 15114, 2012. Fibre-reinforced plastic composites - Determination of the mode II facture resistance for unidirectionally reinforced materials using the calibrated end-loaded split (C-ELS) test and an effective crack length approach.

Jensen, S.M., Bak, B.L.V., Bender, J.J., Carreras, L., Lindgaard, E., 2021a. Transient delamination growth in GFRP laminates with fiber bridging under variable amplitude loading in G-control. Compos. Part B Eng. 225, 109296.

Jensen, S.M., Bak, B.L.V., Bender, J.J., Lindgaard, E., 2021b. Transition-behaviours in fatigue-driven delamination of GFRP laminates following step changes in block amplitude loading. Int. J. Fatigue 144, 106045.

Jiang, W.-G., Hallett, S.R., Green, B.G., Wisnom, M.R., 2007. A concise interface constitutive law for analysis of delamination and splitting in composite materials and its application to scaled notched tensile specimens. Int. J. Numer. Methods Eng. 69, 1982–1995.

Kawashita, L.F., Hallett, S.R., 2012. A crack tip tracking algorithm for cohesive interface

element analysis of fatigue delamination propagation in composite materials. Int. J. Solids Struct. 49, 2898–2913.

Kawashita, L.F., Jones, M.I., Giannis, S., Hallett, S.R., Wisnom, M.R., 2011. High fidelity modelling of tapered laminates with internal ply terminations, in: 18th International Conference on Composite Materials. Jeju Island, Korean, pp. 1–6.

Krueger, R., 2004. Virtual crack closure technique: History, approach, and applications. Appl. Mech. Rev. 57, 109–143.

Latifi, M., van der Meer, F.P., Sluys, L.J., 2015. A level set model for simulating fatigue-driven delamination in composites. Int. J. Fatigue 80, 434–442.

Li, C., Thostenson, E.T., Chou, T.-W., 2008. Sensors and actuators based on carbon nanotubes and their composites: A review. Compos. Sci. Technol. 68, 1227–1249.

Mandell, J.F., Meier, U., 1975. Fatigue crack propagation in 0/90 E-glass/epoxy composites. ASTM STP 569, 28–44.

Mohamed, G., Allegri, G., Yasaee, M., Hallett, S.R., 2018. Cohesive element formulation for z-pin delamination bridging in fibre reinforced laminates. Int. J. Solids Struct. 132–133, 232–244.

Mukhopadhyay, S., Nixon-Pearson, O.J., Hallett, S.R., 2018. An experimental and numerical study on fatigue damage development in laminates containing embedded wrinkle defects. Int. J. Fatigue 107, 1–12.

Nojavan, S., Schesser, D., Yang, Q.D., 2016. An in situ fatigue-CZM for unified crack initiation and propagation in composites under cyclic loading. Compos. Struct. 146, 34–49.

Paepegem, W. Van, Degrieck, J., 2001. Fatigue degradation modelling of plain woven glass/epoxy composites. Compos. - Part A Appl. Sci. Manuf. 32, 1433–1441.

Parrinello, F., Gulizzi, V., Benedetti, I., 2021. A computational framework for low-cycle fatigue in polycrystalline materials. Comput. Methods Appl. Mech. Eng. 383, 113898.

Pascoe, J.A., Alderliesten, R.C., Benedictus, R., 2013. Methods for the prediction of fatigue delamination growth in composites and adhesive bonds - A critical review. Eng. Fract. Mech. 112–113, 72–96.

Pirondi, A., Giuliese, G., Moroni, F., Bernasconi, A., Jamil, A., 2014. Comparative study of cohesive zone and virtual crack closure techniques for three-dimensional fatigue debonding. J. Adhes. 90, 457–481.

Pirondi, A., Moroni, F., 2019. Improvement of a cohesive zone model for fatigue delamination rate simulation. Materials (Basel). 12, 181.

Raimondo, A., Bisagni, C., 2020. Analysis of local stress ratio for delamination in composites under fatigue loads. AIAA J. 58, 455–463.

Rans, C., Alderliesten, R., Benedictus, R., 2011. Misinterpreting the results: How similitude can improve our understanding of fatigue delamination growth. Compos. Sci. Technol. 71, 230–238.

Robinson, P., Galvanetto, U., Tumino, D., Bellucci, G., Violeau, D., 2005. Numerical simulation of fatigue-driven delamination using interface elements. Int. J. Numer. Methods Eng. 63, 1824–1848.

Rouchon, J., 2009. Fatigue and damage tolerance evaluation of structures: the composite materials response, NLR-TP-2009-221, National Aerospace Laboratory NLR.

Salih, S., Davey, K., Zou, Z., 2018. Frequency-dependent cohesive-zone model for fatigue. Int. J. Solids Struct. 152–153, 228–237.

Sarfaraz, R., Vassilopoulos, A.P., Keller, T., 2013. Variable amplitude fatigue of adhesively-bonded pultruded GFRP joints. Int. J. Fatigue 55, 22–32.

Tanaka, H., Tanaka, K., Tsuji, T., Katoh, H., 1999. Mixed-mode (I+II) propagation of delamination fatigue cracks in unidirectional graphite/epoxy laminates. Trans. Japan Soc. Mech. Eng. Ser. A 65, 1676–1683.

Tanaka, K., Tanaka, H., 1997. Stress-ratio effect on mode II propagation of interlaminar fatigue cracks in graphite/epoxy composites. Compos. Mater. Fatigue Fract. (Sixth Vol. ASTM STP 1285 126–142.

Tanaka, K., Tanaka, H., Tsuji, T., Yamagishi, K., 1995. Effect of stress ratio on mode I propagation of interlaminar fatigue cracks in CFRP. J. Soc. Mater. Sci. Japan 44, 960–966.

Tao, C., Mukhopadhyay, S., Zhang, B., Kawashita, L.F., Qiu, J., Hallett, S.R., 2018. An improved delamination fatigue cohesive interface model for complex three-dimensional multi-interface cases. Compos. Part A Appl. Sci. Manuf. 107, 633–646.

Turon, A., Costa, J., Camanho, P.P., Dávila, C.G., 2007. Simulation of delamination in composites under high-cycle fatigue. Compos. Part A Appl. Sci. Manuf. 38, 2270–2282.

Williams, J.G., 1988. On the calculation of energy release rates for cracked laminates. Int. J. Fract. 36, 101–119.

Zhang, B., Kawashita, L.F., Hallett, S.R., 2020a. Composites fatigue delamination prediction using double load envelopes and twin cohesive models. Compos. Part A Appl. Sci. Manuf. 129, 105711.

Zhang, B., Kawashita, L.F., Jones, M.I., Lander, J.K., Hallett, S.R., 2020b. An experimental

and numerical investigation into damage mechanisms in tapered laminates under tensile loading. Compos. Part A Appl. Sci. Manuf. 133, 105862.

Zhang, Z., Friedrich, K., 2003. Artificial neural networks applied to polymer composites: a review. Compos. Sci. Technol. 63, 2029–2044.

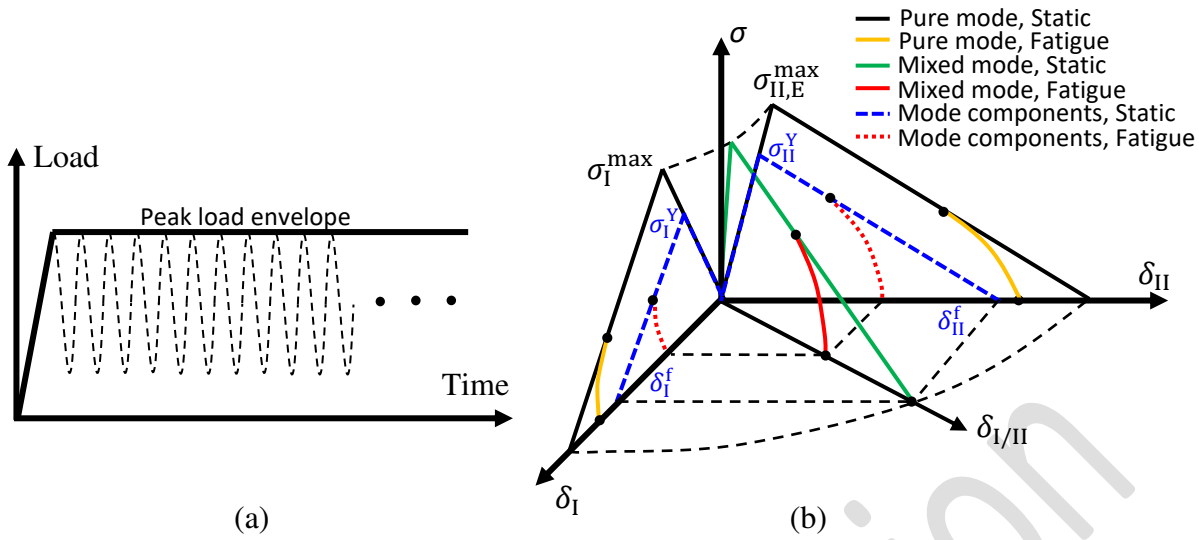

Fig. 1. (a) Load envelope and (b) mixed-mode bilinear static and fatigue cohesive law for fatigue delamination prediction.

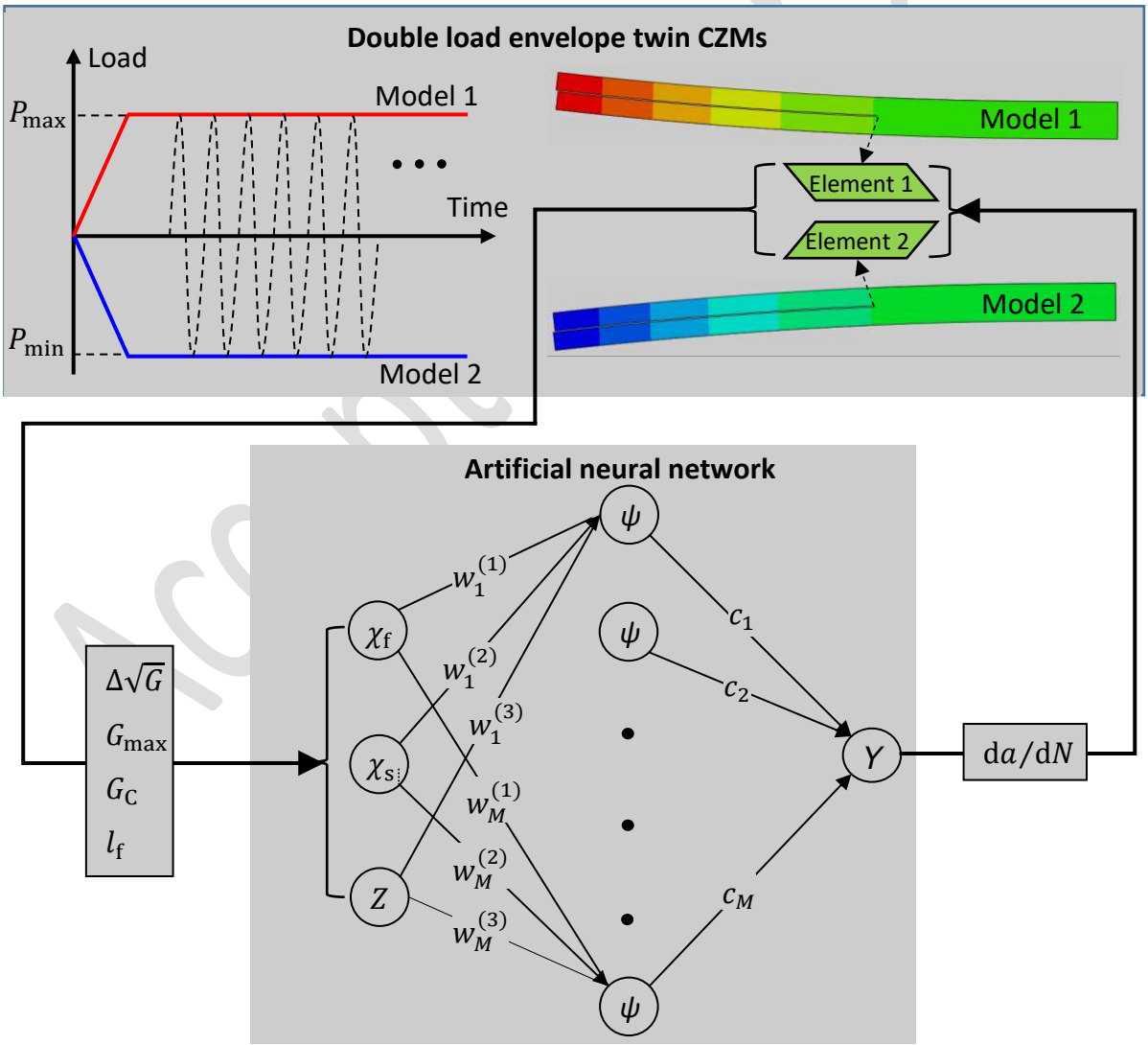

Fig. 2. Fatigue delamination growth prediction by the combination of double load envelope twin CZMs and an artificial neural network.

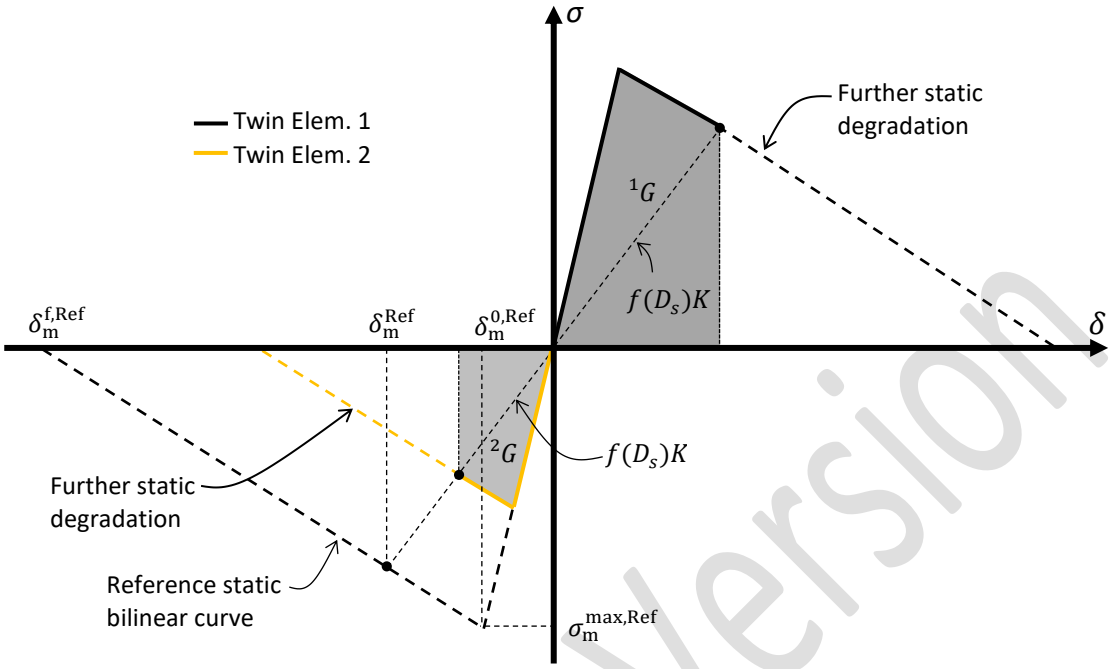

Fig. 3. Typical traction versus displacement relations of two twin cohesive elements in the load build-up stage of a partially reversed mode II fatigue model.

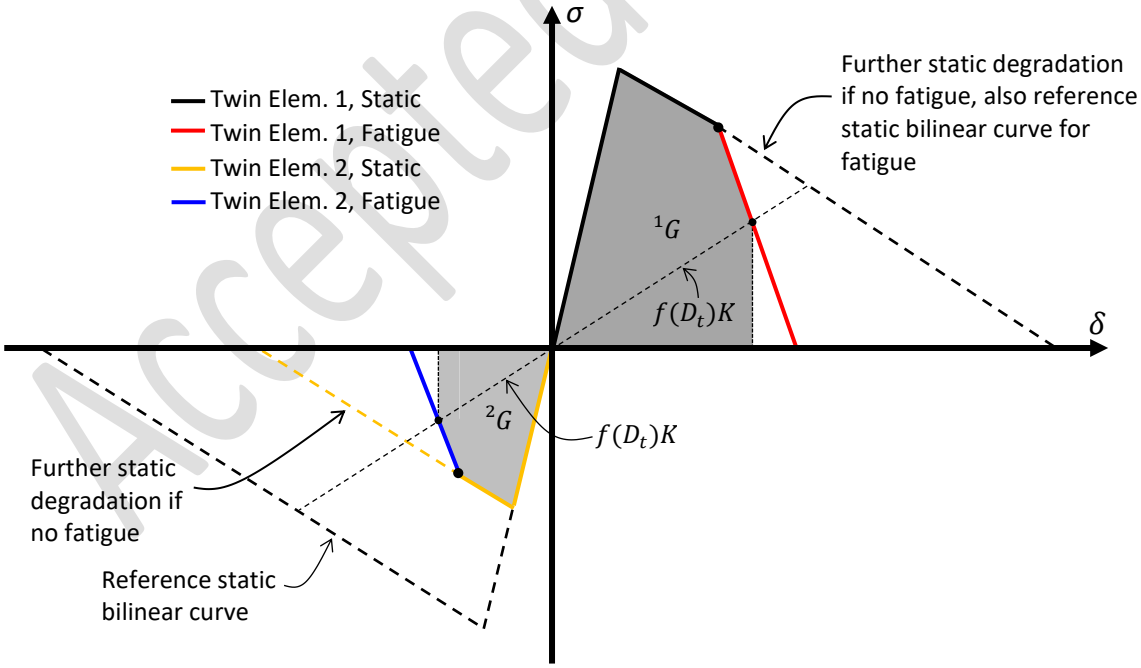

Fig. 4. Typical traction versus displacement relations of two twin cohesive elements in the fatigue stage of a partially reversed mode II fatigue model.

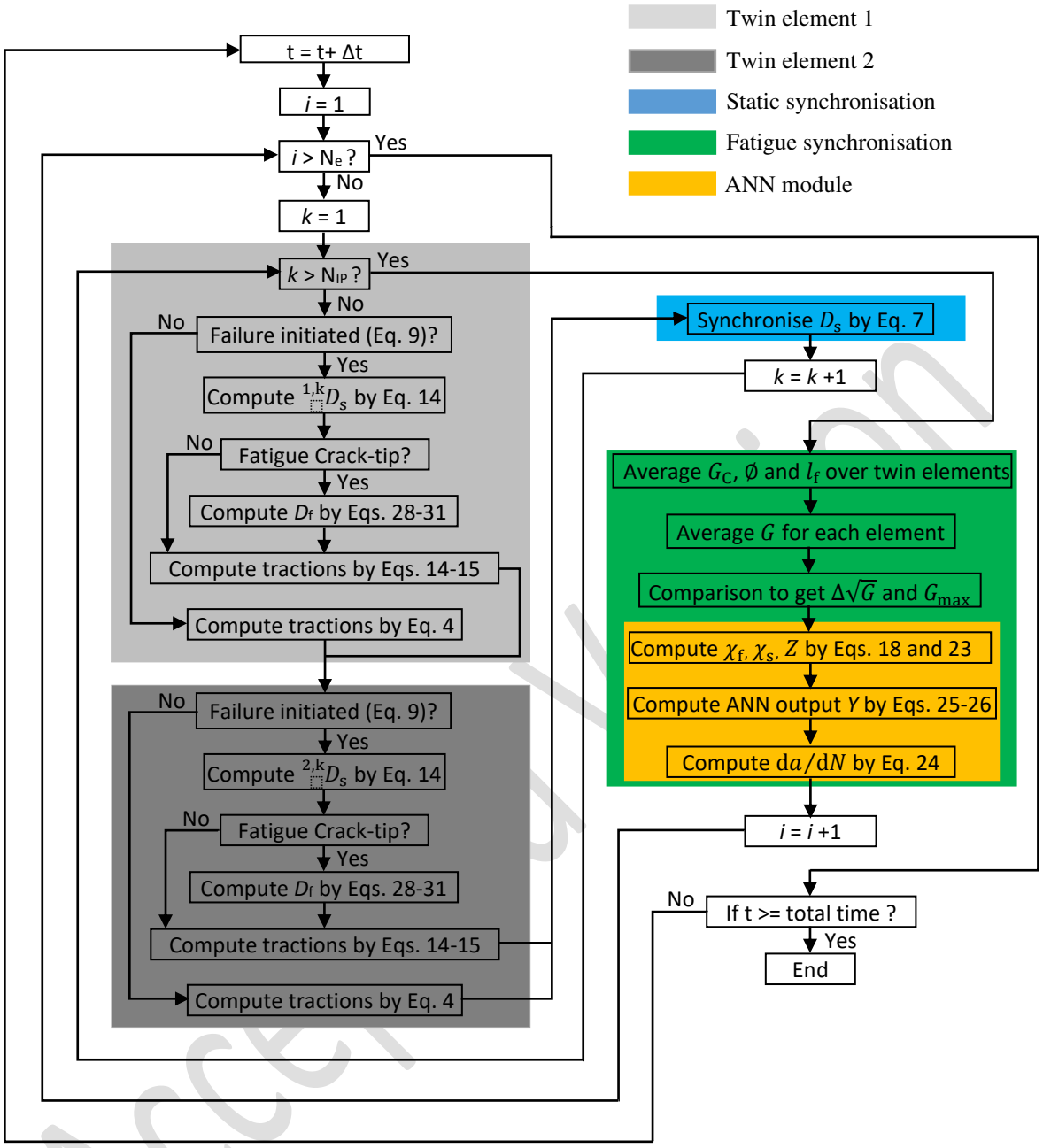

Fig. 5. Workflow of implementing the fatigue cohesive formulation by an Abaqus/Explicit VUMAT subroutine on one core; N_e is the number of cohesive element pairs; N_{IP} is the number of integration points owned by a cohesive element, and it is four when the Abaqus COH3D8 element used.

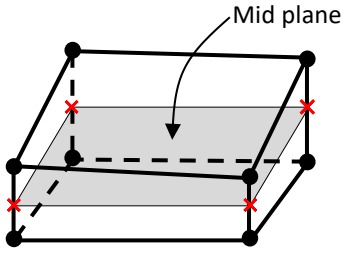

Fig. 6. A 4-IP COH3D8 cohesive element in Abaqus (node in block dot and IP in cross).

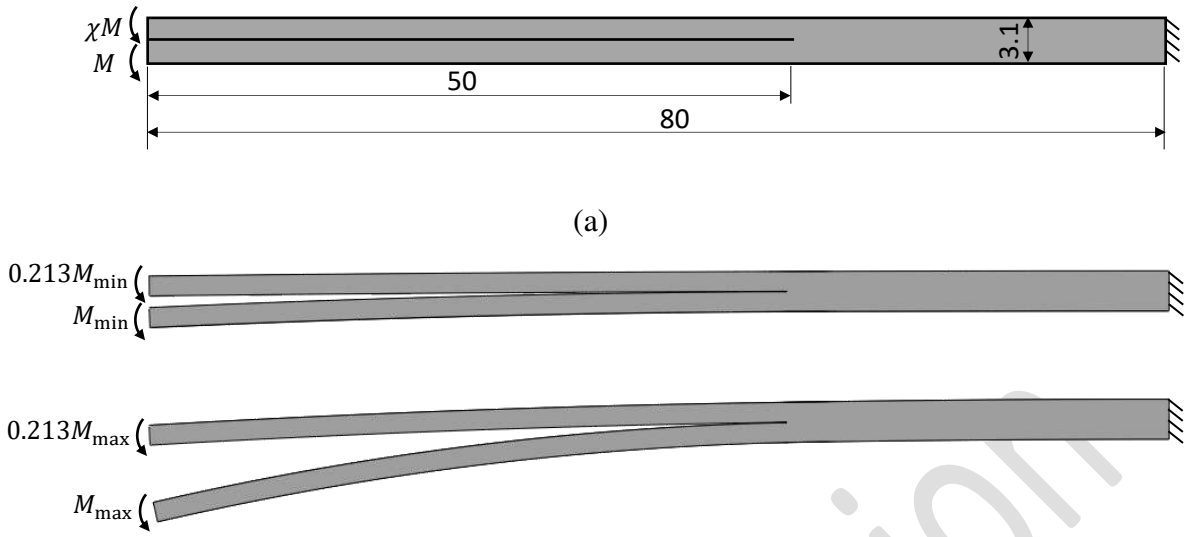

Fig. 7. (a) Side view of the edge cracked cantilever laminate used for assessing the fatigue CZMs (unit: mm), and (b) boundary definitions of the twin cohesive models in the 0.64 MMB case with $R = 0.2$.

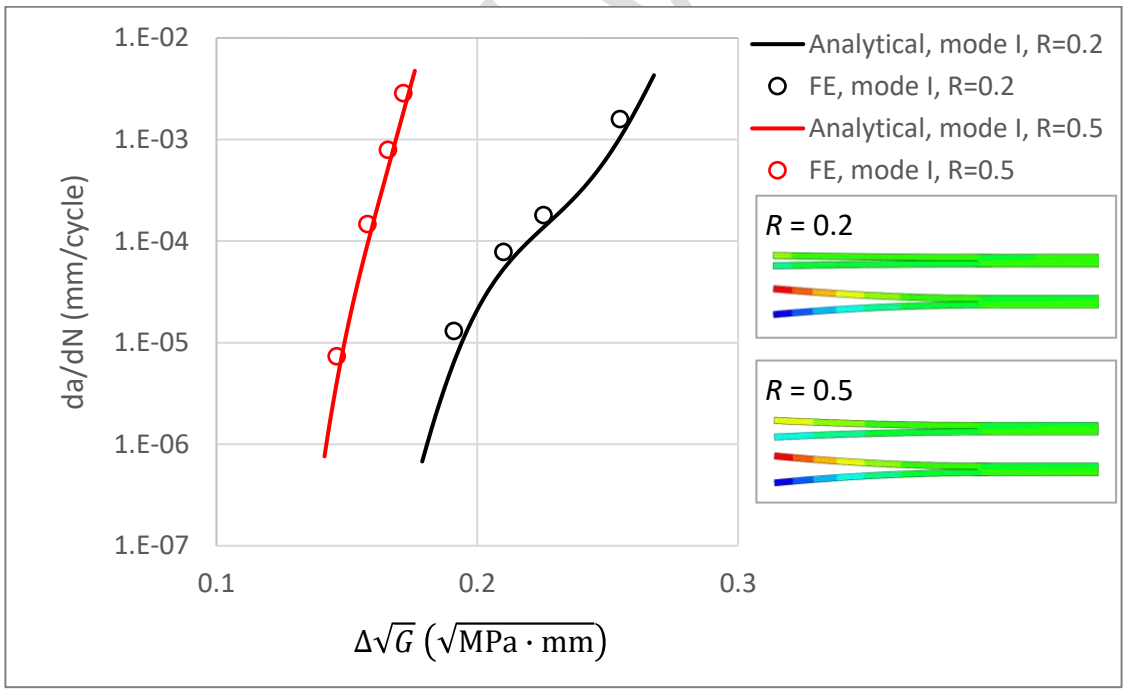

Fig. 8. Comparison between analytical solutions and FE predictions regarding mode I fatigue crack growth rate.

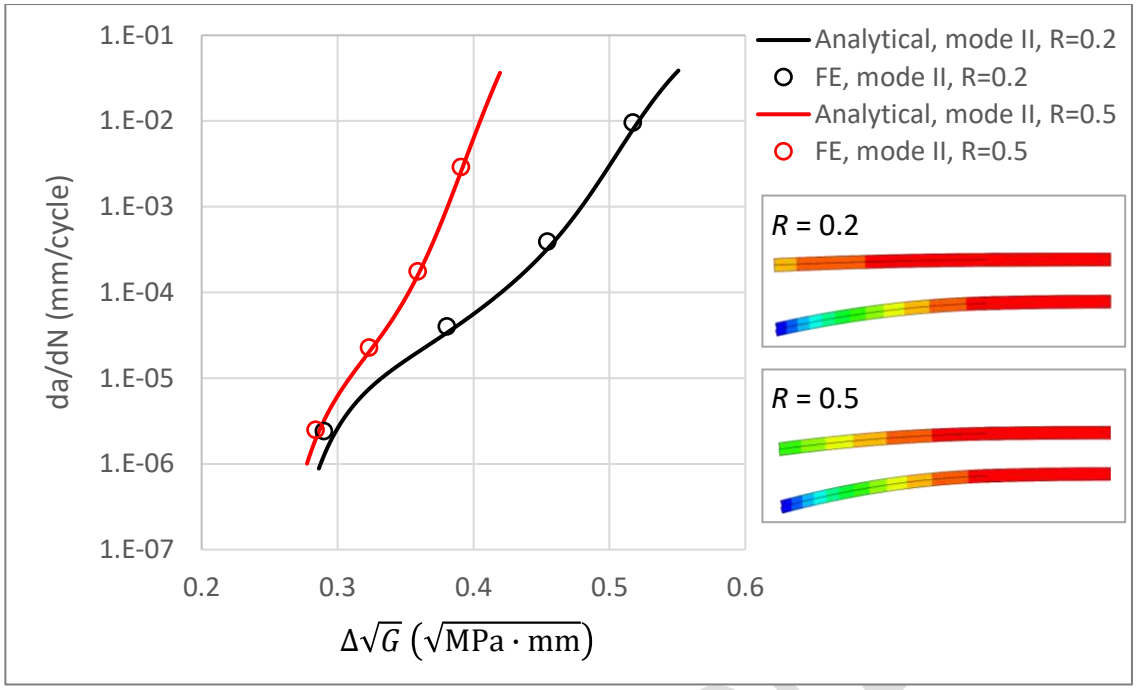

Fig. 9. Comparison between analytical solutions and FE predictions regarding mode II fatigue crack growth rate without load reversal.

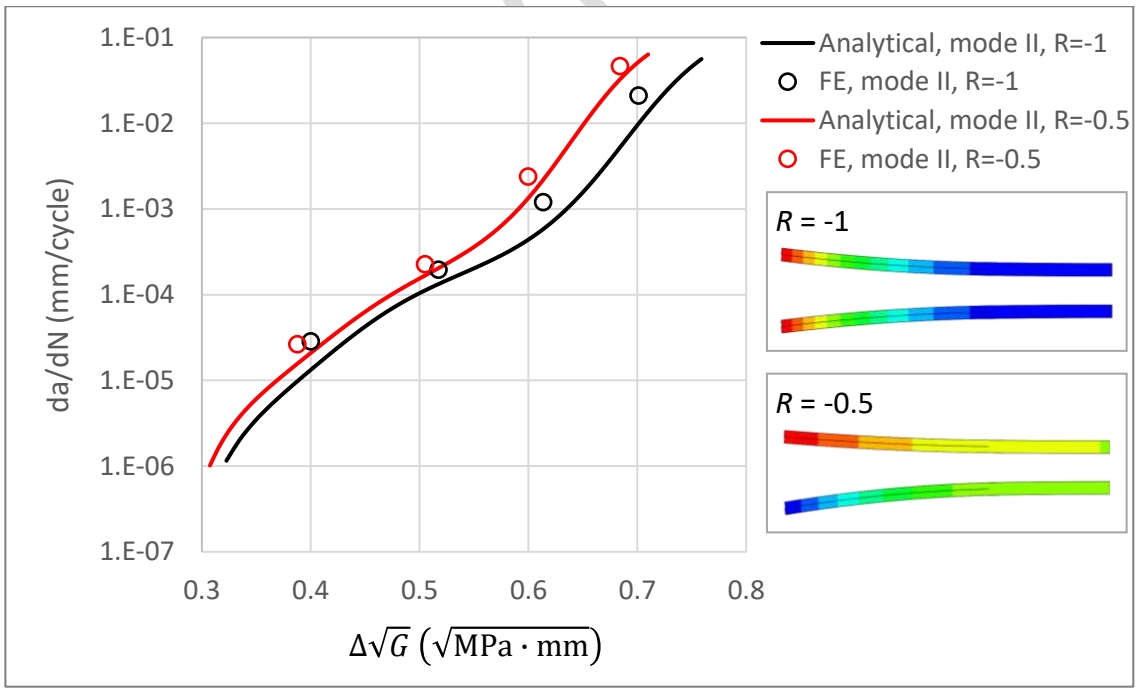

Fig. 10. Comparison between analytical solutions and FE predictions regarding mode II fatigue crack growth rate with load reversal.

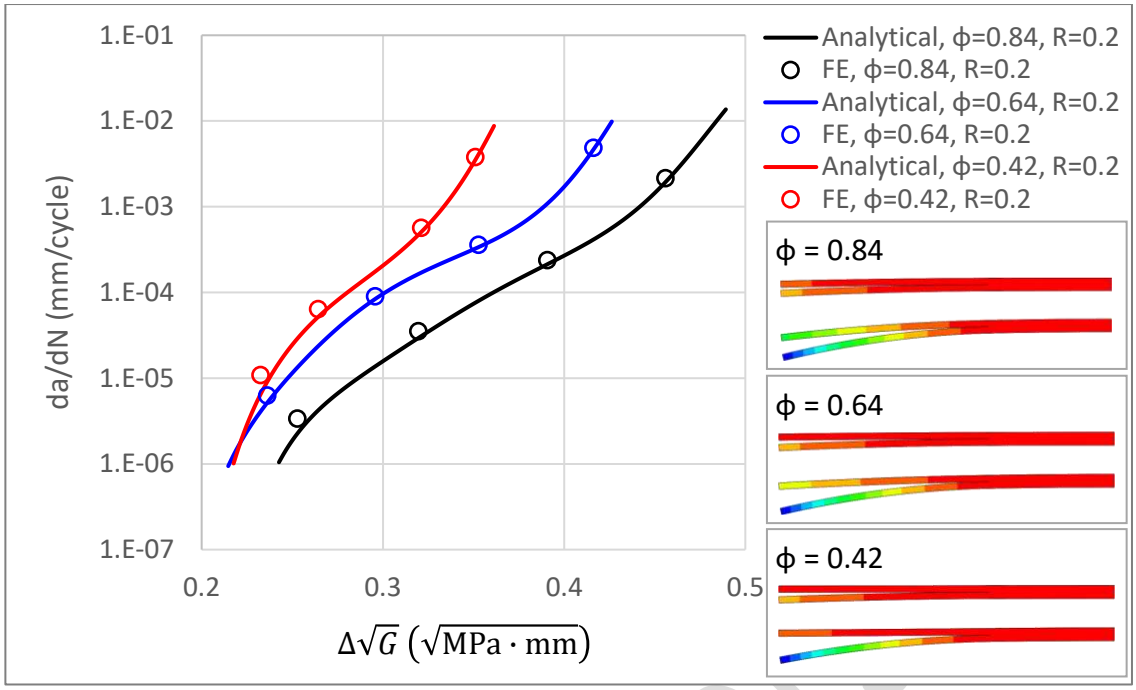

Fig. 11. Comparison between analytical solutions and FE predictions regarding mixed-mode fatigue crack growth rate.

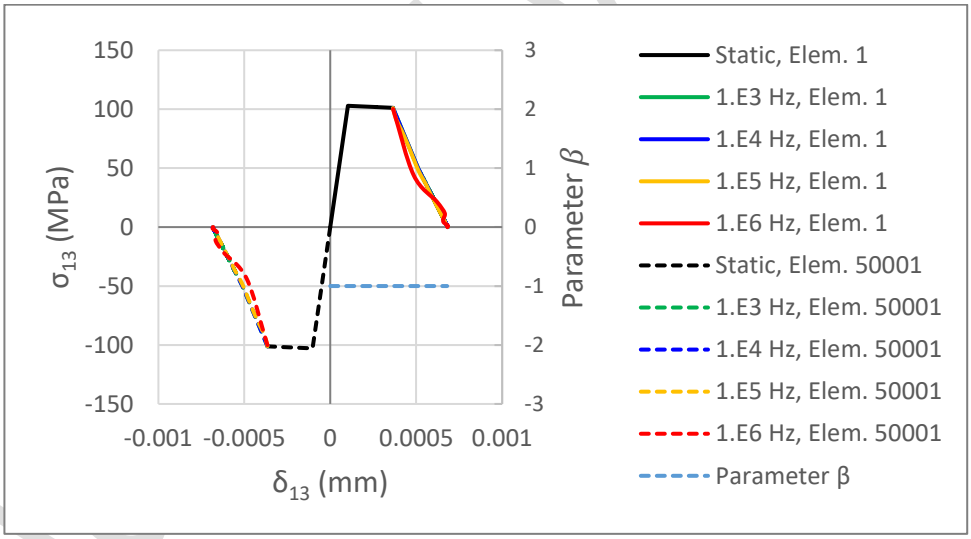

Fig. 12. Effects of numerical fatigue frequency on the traction versus displacement relationships of the initial crack-tip twin elements (element 1 and element 50001) in the 5% G_{max}/G_C ratio and $R = -1$ model.

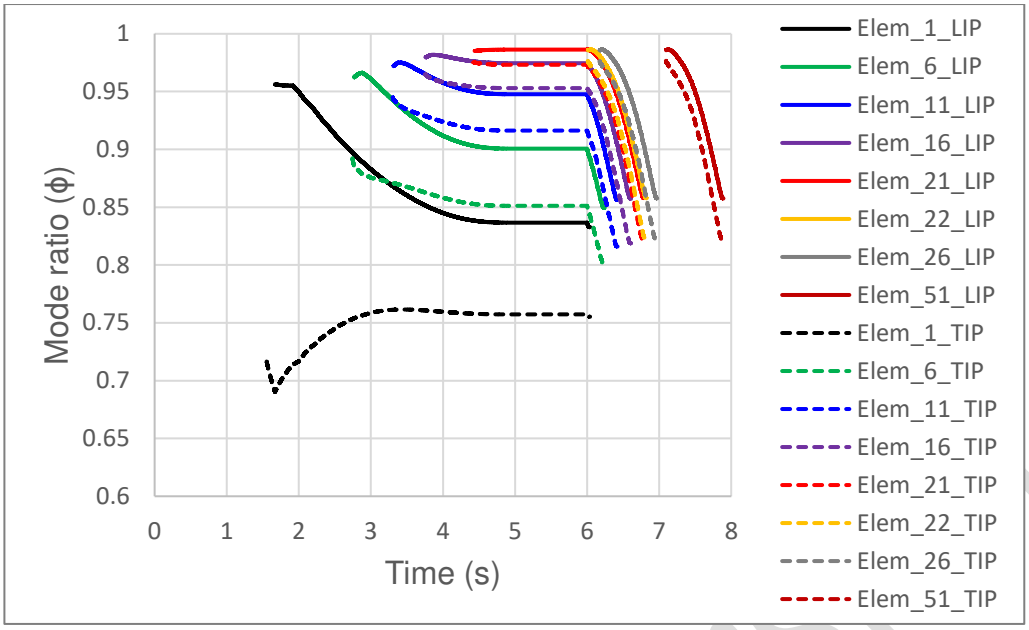

(a)

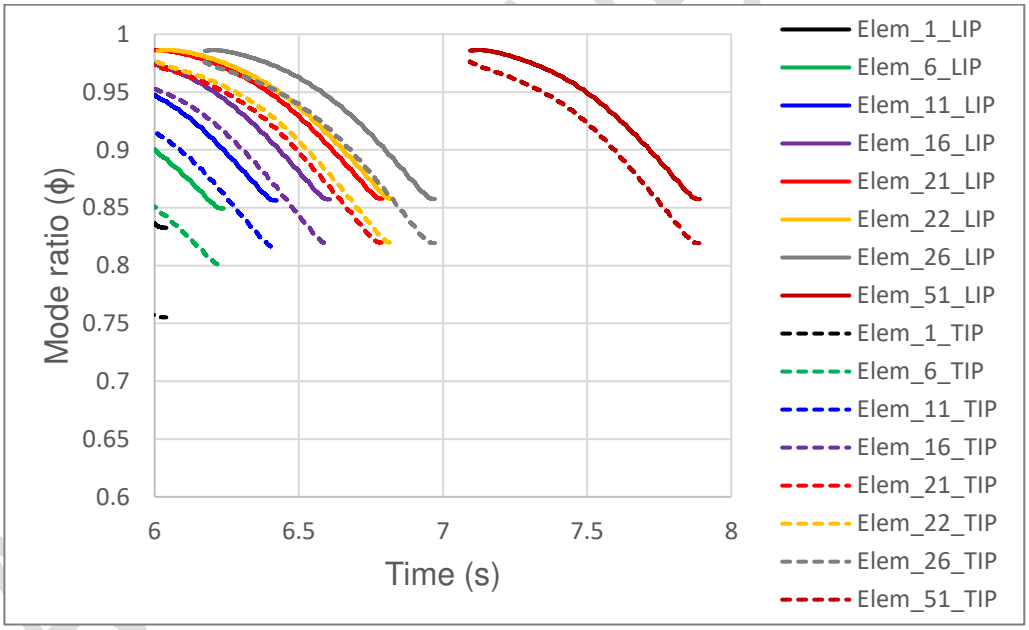

(b)

Fig. 13. Mode ratio plots for the leading IPs (solid lines) and trailing IPs (dashed lines) of selected elements from the initial crack tip in the peak-load model of the 55% $G_{\max}/G_C$ ratio and 0.84 MMB case: (a) overall plots for static, load-holding and fatigue stages and (b) localised plots for the fatigue stage; 'LIP' is the abbreviation for 'leading integration point', and 'TIP' for 'trailing integration point'.

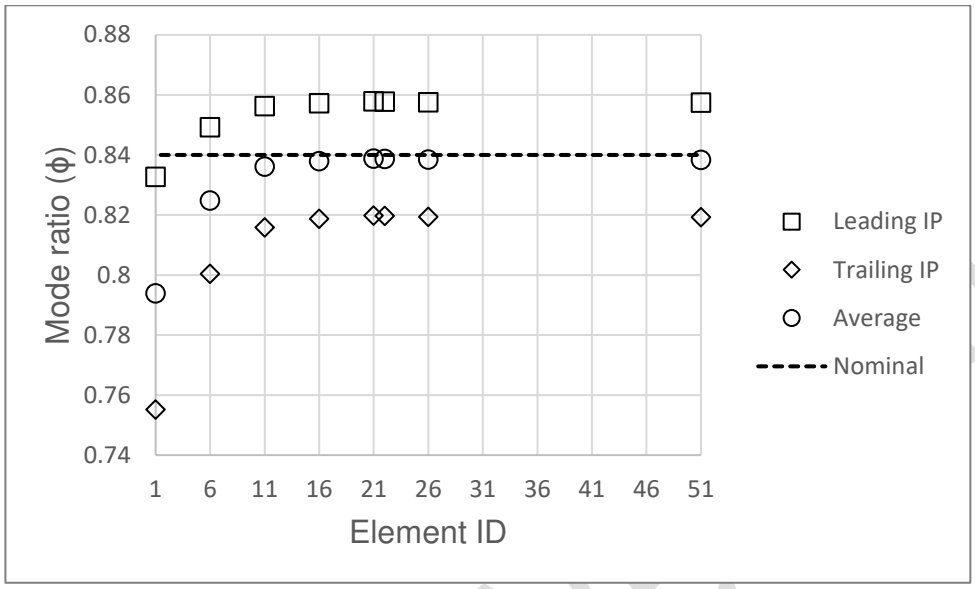

Fig. 14. Mode ratio at full failure in the peak-load model of the 55% $G_{\max}/G_{\mathrm{C}}$ ratio and 0.84 MMB case.

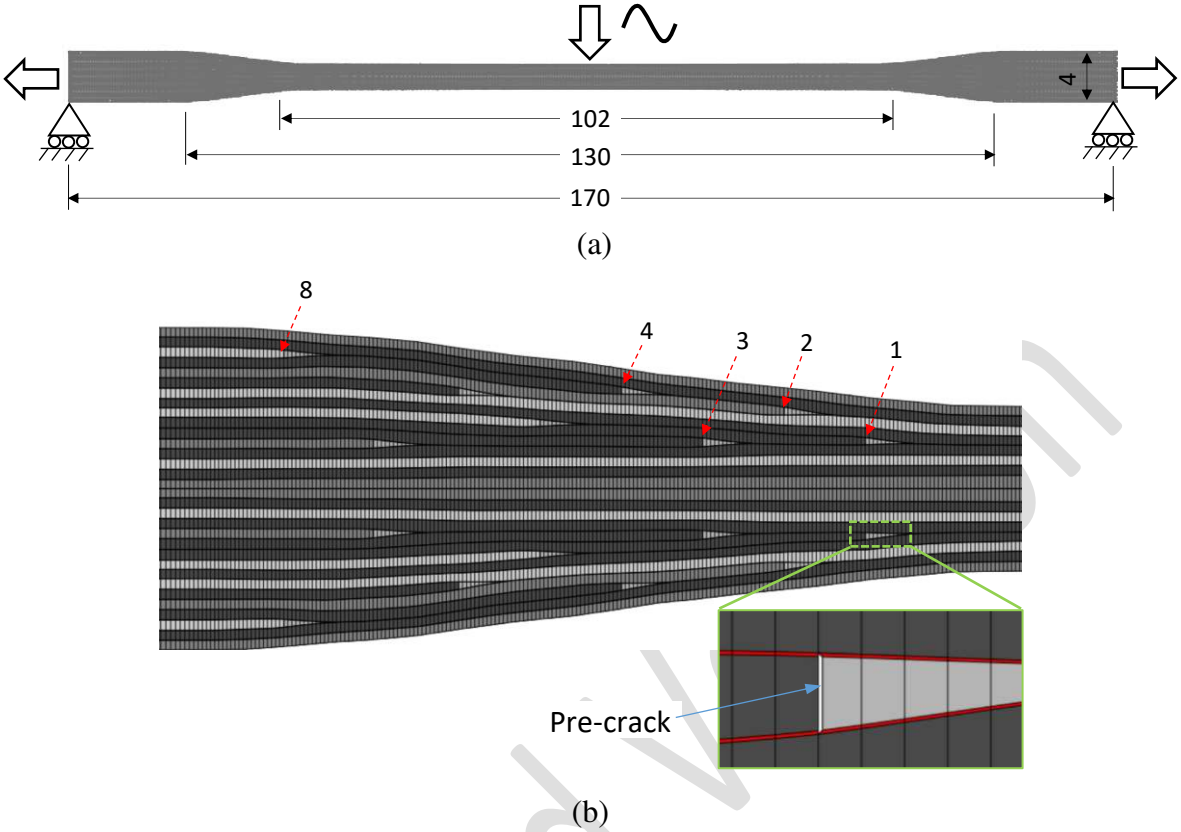

Fig. 15. (a) Schematic of the double-side tapered laminate subjected to static tension and cyclic bending (unit: mm) and (b) finite element mesh of the tapered section.

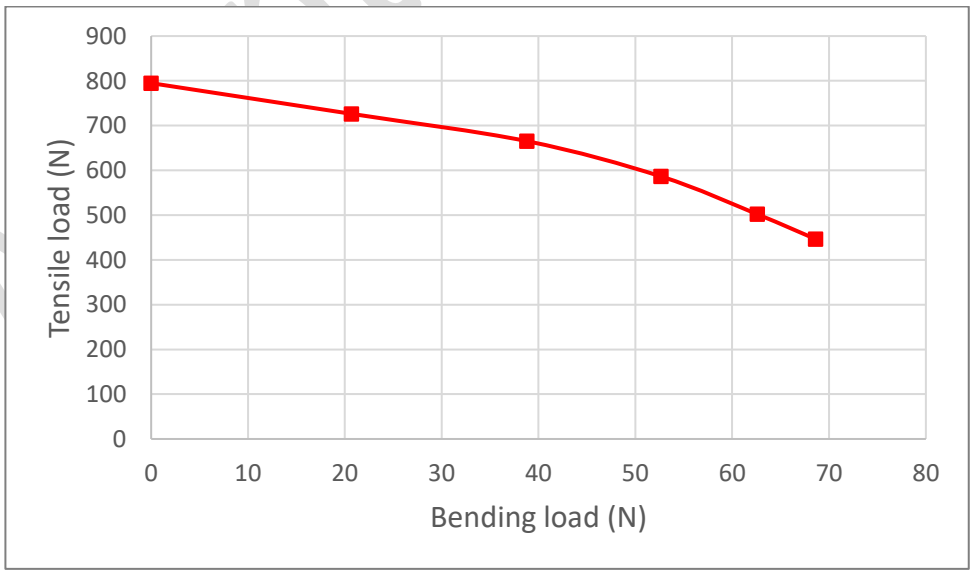

Fig. 16. Static failure envelope of the virtual tapered laminate under combined tension and bending.

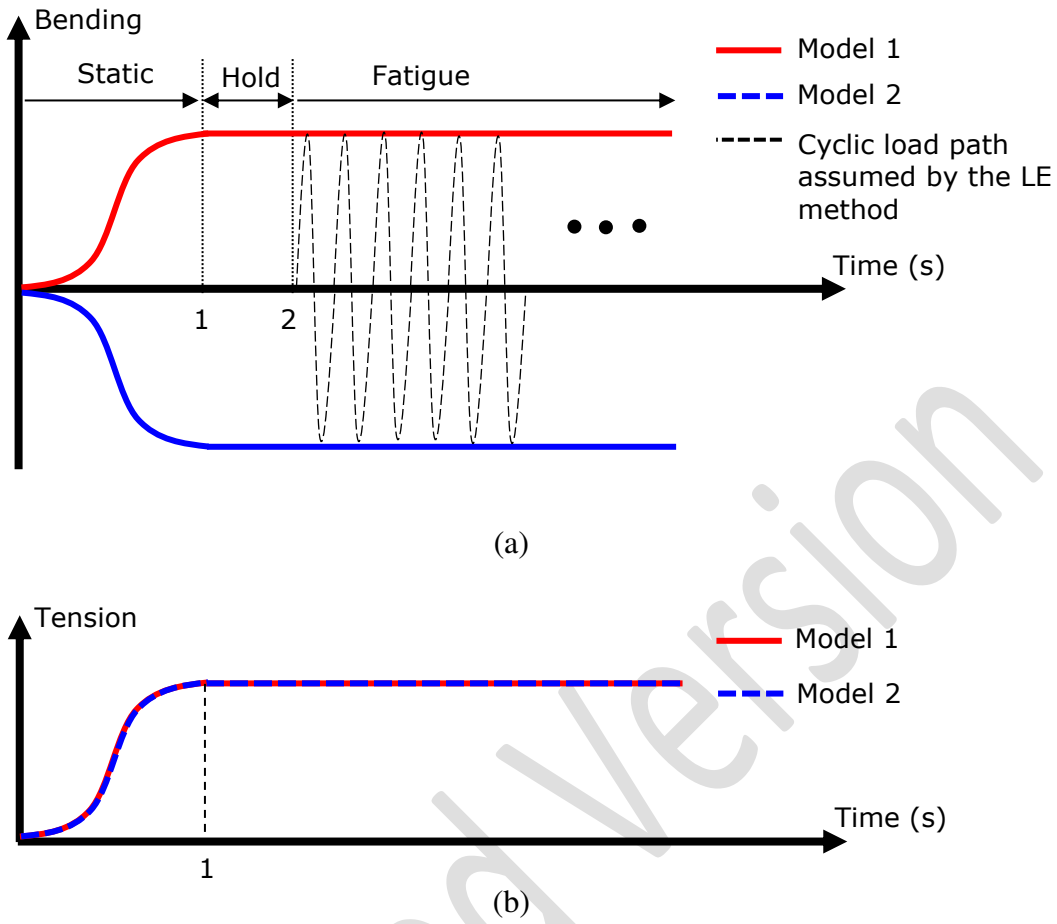

Fig. 17. The load histories of the twin cohesive models for (a) bending and (b) tension.

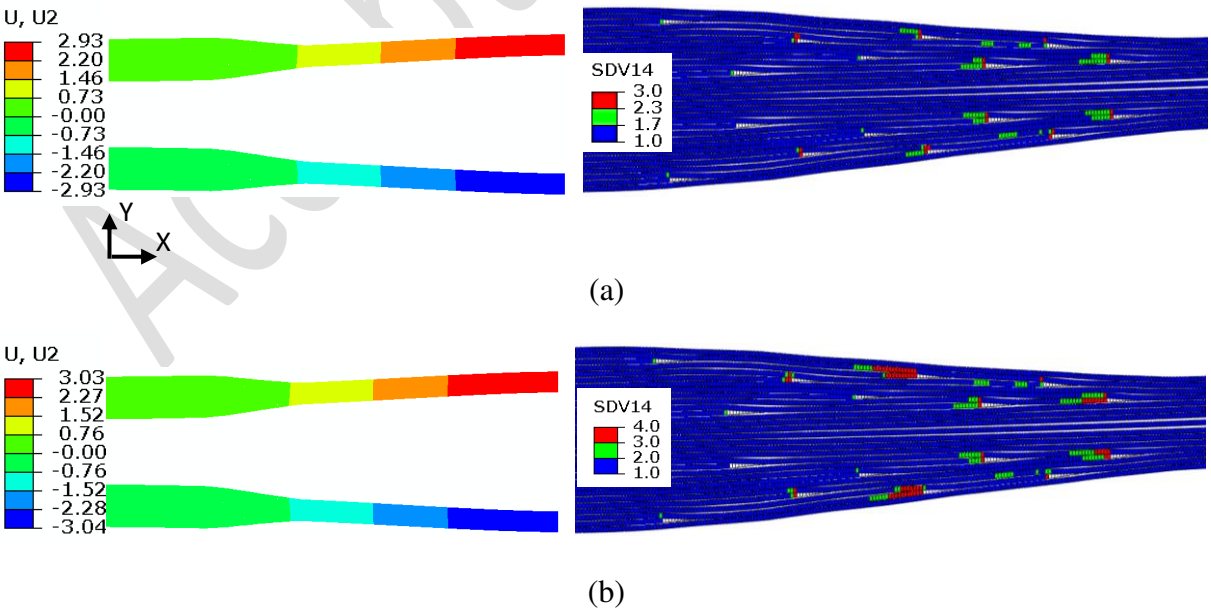

Fig. 18. Deformation and interface failure status of the -1 bending *R* ratio models (a) at the start of fatigue loading and (b) at the 2100-th cycle; SDV14 is the cohesive failure flag (1-elastic, 2- static degradation, 3- fatigue degradation, 4-full failure).

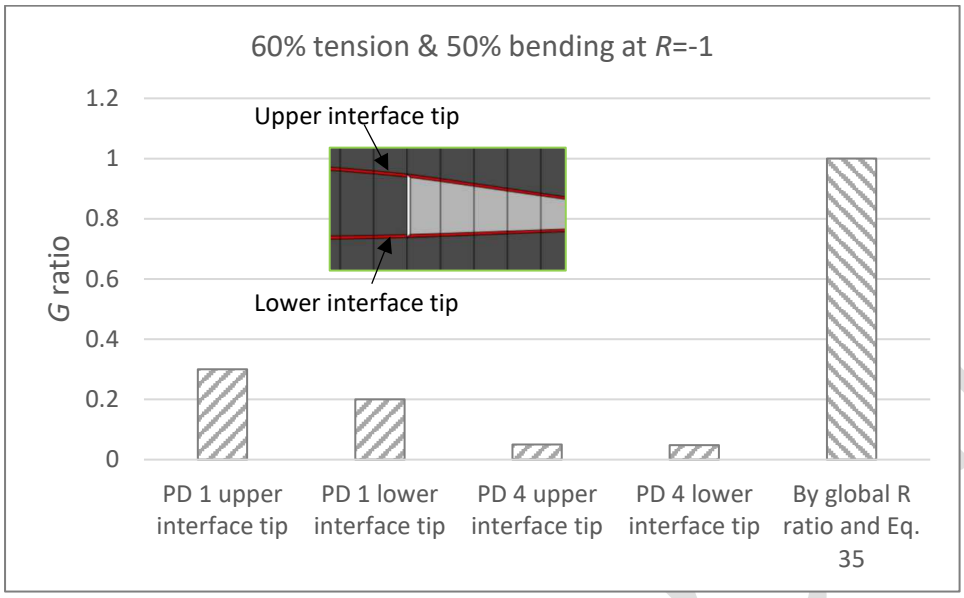

(a)

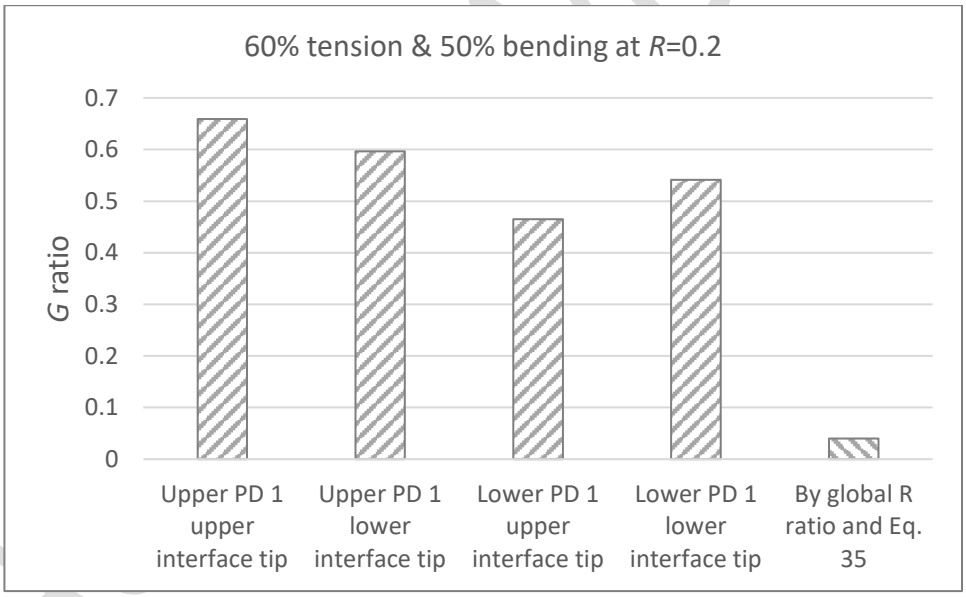

(b)

Fig. 19. Energy release rate (G) ratios achieved by the twin cohesive elements at selected ply drops in comparison with the G ratios derived by the global R ratio and Eq. 35; 'PD' is the abbreviation for 'ply drop'.

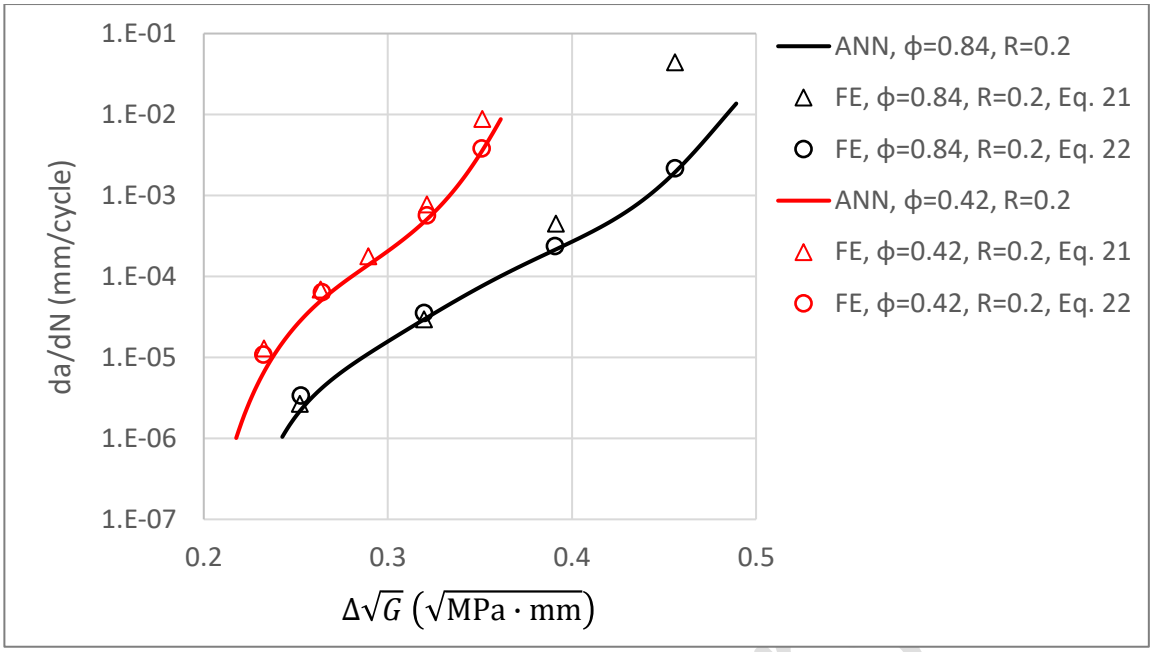

Fig. 20. Comparison between two G_C estimate approaches (Eq. 21 and Eq. 22) regarding prediction of mixed-mode fatigue crack growth rates.

Table 1. Material properties for T800H/#3631.

Ply properties		**Interface properties**	
E_{11} (MPa)	137,000	G_{IC} (N/mm)	0.18
$E_{22} = E_{33}$ (MPa)	8,100	G_{IIC} (N/mm)	0.821
$G_{12} = G_{13}$ (MPa)	4,800	σ_{I}^{max} (MPa)	69.6
G_{23} (MPa)	2,613	σ_{II}^{max} (MPa)	102.9
$\nu_{12} = \nu_{13}$	0.31	K_I (N/mm^3)	1×10^6
ν_{23}	0.55	K_{II} (N/mm^3)	1×10^6
		α	1
		η	0.3

Table 2. Inner weights, activation thresholds and outer weights of the ANN.

j	$w_j^{(1)}$	$w_j^{(2)}$	$w_j^{(2)}$	b_j	c_j
1	0.234	-5.314	1.430	4.364	0.132
2	-6.518	17.157	-3.845	-13.555	-0.028
3	1.187	-14.796	-6.064	-2.252	8.605
4	8.060	-2.835	12.022	24.104	0.104
5	-2.233	3.052	-13.918	-7.436	-0.006
6	-0.787	4.050	5.013	2.188	-0.507
7	-3.776	8.886	10.374	-2.141	-0.086
8	3.326	-4.155	-4.550	-0.115	0.020
9	2.115	-1.296	14.535	1.635	0.314
10	-6.824	9.395	-11.774	-1.596	-0.152
11	-9.807	0.317	3.792	-10.390	-81.729
12	0.693	-11.998	0.873	-11.733	3401.781
13	7.350	-0.848	-3.109	0.058	0.123
14	11.431	-1.176	1.014	17.417	0.096
15	2.019	-0.050	7.293	-2.990	0.106
16	-4.267	2.101	5.896	-2.282	-0.120
17	0.843	-1.753	3.790	11.130	0.105
18	6.621	-7.447	9.983	-14.414	1.295